SURFACE ENHANCED RAMAN SPECTROSCOPY OF THE PLASMONIC
NANOGRATINGS OBTAINED BY LASER INDUCED PERIODIC SURFACE
STRUCTURING

A THESIS SUBMITTED TO
THE GRADUATE SCHOOL OF NATURAL AND APPLIED SCIENCES
OF
MIDDLE EAST TECHNICAL UNIVERSITY

BY

SERENA NUR ERKIZAN

IN PARTIAL FULFILLMENT OF THE REQUIREMENTS
FOR
THE DEGREE OF MASTER OF SCIENCE
IN
PHYSICS

JANUARY 2023

Approval of the thesis:

SURFACE ENHANCED RAMAN SPECTROSCOPY OF THE PLASMONIC NANOGRATINGS OBTAINED BY LASER INDUCED PERIODIC SURFACE STRUCTURING

submitted by **SERENA NUR ERKIZAN** in partial fulfillment of the requirements for the degree of **Master of Science** in **Physics, Middle East Technical University** by,

Prof. Dr. Halil Kalıpçılar
Dean, Graduate School of **Natural and Applied Sciences**   _____

Prof. Dr. Seçkin Kürkcüoğlu
Head of the Department, **Physics**   _____

Prof. Dr. Alpan Bek
Supervisor, **Physics, METU**   _____

Examining Committee Members:

Prof. Dr. Gökhan Demirel
Chemistry Department, Gazi University   _____

Prof. Dr. Alpan Bek
Physics Department, METU   _____

Assoc. Prof. Dr. Hande Toffoli
Physics Department, METU   _____

Date: 31.01.2023

I hereby declare that all information in this document has been obtained and presented in accordance with academic rules and ethical conduct. I also declare that, as required by these rules and conduct, I have fully cited and referenced all material and results that are not original to this work.

Name Last name : Serena Nur Erkızan

Signature :

ABSTRACT

SURFACE ENHANCED RAMAN SPECTROSCOPY OF THE PLASMONIC NANOGRATINGS OBTAINED BY LASER INDUCED PERIODIC SURFACE STRUCTURING

Erkızan, Serena Nur
Master of Science, Physics
Supervisor : Prof. Dr. Alpan Bek

January 2023, 80 pages

The research conducted in this study presents a novel method of generating highly sensitive Surface Enhanced Raman Spectroscopy (SERS) substrates by femtosecond laser writing techniques. Two different types of periodicity regimes are introduced by femtosecond laser-based nano-structuring of crystalline Silicon (Si) and generated patterns are classified as Low Spatial Frequency LIPSS (LSFL) and High Spatial Frequency LIPSS (HSFL). Quasi periodic, self-organized femtosecond laser written periodic nanostructures can embody required plasmonic gap distance, roughness and randomness to accommodate high hotspot density and enhancement factor of SERS. Silver (Ag) deposited nanoripples with different periodicity regimes exhibit state of art SERS enhancement factor as high as 10^9 with 10^{-11} M limit of detection for Crystal Violet (CV) molecule. Enhancement factor dependence of the SERS substrates is investigated at Raman excitation wavelength 532, 660 and 785 nm. Raman enhancement factor simulations for all excitation wavelengths are performed by Finite Elements Method (FEM) based Maxwell solver by using COMSOL Multiphysics. Enhancement factor results obtained by measured SERS spectra and electric field enhancement simulations exhibit good agreement between them. A major advantage introduced by femtosecond laser-based SERS substrates is

accurate and flexible control of processed region without restricting processing over large areas compared to well established top-down approaches such as nanoimprint lithography, electron beam lithography, chemical plasma etching. Fs-nanoripple generation do not require multiple processing steps like in nanoimprint lithography including stamp production of nanostructures, pattern transfer and peeling off. On the contrary of chemically synthesized and aggregated nanoparticle colloids, metal deposited quasi-periodic nanoripples offer reproducibility of obtained SERS signal over large areas and chemical stability for SERS aging measurements.

Keywords: Surface Enhanced Raman Scattering, Femtosecond Laser Induced Periodic Surface Structuring

ÖZ

LAZERLE PERİYODİK YÜZEY YAPILANDIRMASI İLE ELDE EDİLEN PLAZMONİK NANO-KIRINIM AĞLARININ YÜZEY ARTIRIMLI RAMAN SPEKTROSKOPİSİ

Erkızan, Serena Nur
Yüksek Lisans, Fizik
Tez Yöneticisi: Prof. Dr. Alpan Bek

Ocak 2023, 80 sayfa

Bu çalışma yüksek hassaslıkta çalışan Yüzey Artırımlı Raman Spektroskopi (YARS) örneklerinin femtosaniye lazer işleme teknikleri ile üretilmesini ele almaktadır. Silikon yüzeyin femtosaniye lazer kaynaklı nano yapılandırılmasıyla iki farklı periyodik rejimde yüzey yapısı üretilmiş ve Düşük Uzamsal Frekanslı Periyodik Yüzey Yapısı (DUFPY) ve Yüksek Uzamsal Frekanslı Periyodik Yüzey Yapısı (YUFPY) olarak sınıflandırılmıştır. YARS örneğinde yüksek elektrik alan artırımına sahip faal nokta yoğunluğunun artışı ve artırım faktörü (AF) değerinin yükselmesi için gereken plazmonik aralık mesafesi, pürüzlülük femtosaniye lazer ile oluşturulmuş kısmi periyodik, öz-organize yüzeyler ile sağlanır. İki farklı periyottaki gümüş kaplanmış nano dalgacıklı yapılar ile Crystal Violet (CV) molekülü için literatürdeki son model artırım faktörü değerine 10^9 ve tespit kapasitesi limitine (TKL) 10^{-11} M ulaşılmıştır. Artırım faktörü değeri üç ayrı Raman uyarım dalga boyunda 532, 660 ve 785 nm için deney ve simülasyon sonuçlarıyla incelenmiştir ve bu sonuçlar kendi arasında tutarlıdır. Femtosaniye lazer ile yapılandırılmış YARS örneklerinde öne çıkan en büyük avantaj kontrollü ve yüksek hassasiyetli yapılandırmanın diğer yüksek maliyetli yapılandırma tekniklerine kıyasla geniş yüzey alanlarında da gerçekleştirilebilir olmasıdır.

Anahtar Kelimeler: Yüzey Artırımlı Raman Saçılımı, Femtosaniye Lazerle Periyodik Yüzey Yapılandırması

To my family...

ACKNOWLEDGMENTS

First, I would like to express my deepest gratitude to my advisor Prof.Dr. Alpan Bek for his guidance and endless support throughout my undergraduate study and my Master's. The word "grateful" is an understatement.

I have also been fortunate to have been mentored by Özge Demirtaş, and Nardin Avishan. Chapter 4 and Chapter 5 of this thesis have used material from the publication *LIPSS for SERS: Metal Coated Direct Laser Written Periodic Nanostructures for Surface Enhanced Raman Spectroscopy.* Thanks are owed to the authors of this publication.

I have been very lucky to share my time in *Nano-Optics Research Group* with my friends Ceren Korkut, Alp Akbıyık, Hüseyin Umut Tepe, Murat Öztürk. I thank them for their support and friendship.

I offer my thanks and gratitude to my friends Merve Atlıoğlu, Özgür Uyar, Sinan Çelik, Yankı Yolsever, Giray Mecit, Eylül Öcal for unconditional support and true friendship.

My deepest gratitude is to my parents Hatice Nur and Levent. From the very beginning you have taught me how to reason, to analyse and to wonder. They provided me plenty of encouragement to pursue my dreams. Working for my master was not easy for me with all the life challenges but you were always there to guide and support me. My beloved grandmother's wisdom and cheerfulness will always be in my memories.

"It is not easy to be continuously active in solitude, but with others and towards others it is easier" *Aristotle-Nicomachean Ethics 1170a-5*

TABLE OF CONTENTS

LIST OF TABLES

LIST OF FIGURES

FIGURES

LIST OF ABBREVIATIONS

SERS   Surface Enhanced Raman Spectroscopy

LIPSS   Laser Induced Periodic Surface Structuring

LSP   Localized Surface Plasmons

SPP   Surface Plasmon Polariton

LSPR   Localized Surface Plasmon Resonance

EM   Electromagnetic Field Enhancement

CM   Chemical Enhancement

CV   Crystal Violet

BCB   Brilliant Cresyl Blue

LOD   Limit of Detection

CW   Continuous Wave

HSFL   High Spatial Frequency LIPSS

LSFL   Low Spatial Frequency LIPSS

FTDT   Finite-Difference Time-Domain

AFM   Atomic Force Microscopy

SEM   Scanning Electron Microscopy

DF   Dark Field

RIE   Reactive Ion Etching

MACE   Metal Assisted Chemical Etching

PIERS   Photo Induced Enhanced Raman Spectroscopy

CHAPTER 1

INTRODUCTION

1.1   Thesis Overview

The research and results of this thesis present a novel method of generating highly sensitive Surface Enhanced Raman Spectroscopy (SERS) substrates by femtosecond laser writing techniques. Two different types of periodicity regimes are introduced by femtosecond laser-based nano-structuring of crystalline Silicon (Si) and generated patterns are classified as Low Spatial Frequency LIPSS (LSFL) and High Spatial Frequency LIPSS (HSFL). Quasi periodic, self-organized femtosecond laser written periodic nanostructures can embody required plasmonic gap distance, roughness, and randomness to accommodate high hotspot density and enhancement factor of SERS. Silver (Ag) deposited nanoripples with different periodicity regimes exhibit state of art SERS enhancement factor as high as 10^9 with 10^{-11} M limit of detection for Crystal Violet (CV) molecule. Enhancement factor dependence of the SERS substrates is investigated at Raman excitation wavelength 532, 660 and 785 nm. Raman enhancement factor simulations for all excitation wavelengths are performed by Finite Elements Method (FEM) based Maxwell solver by using COMSOL Multiphysics. Enhancement factor results obtained by measured SERS spectra and electric field enhancement simulations exhibit good agreement between them. The contribution of Localized Surface Plasmons (LSPs) coupled at the far field that might profoundly increase the quality factor of the resonance is analysed by dark field scattering spectra of the SERS substrates. Introduced enhancement factor values in this research present SERS performance that can compete with nanoparticle colloids, nanostructured plasmonic surfaces, and 3D hybrid SERS substrates presented in the literature. A major advantage introduced by femtosecond laser-

based SERS substrates is accurate and flexible control of processed region without restricting processing over large areas compared to well established top-down approaches such as nanoimprint lithography, electron beam lithography, chemical plasma etching [1-3]. Fs-nanoripple generation do not require multiple processing steps like in nanoimprint lithography including stamp production of nanostructures, pattern transfer and peeling off. On the contrary of chemically synthesized and aggregated nanoparticle colloids, metal deposited quasi-periodic nanoripples offer reproducibility of obtained SERS signal over large areas and chemical stability for SERS aging measurements.

Highly sensitive SERS substrates play a crucial role for trace detection or even a single molecule detection of organic and inorganic molecules in a variety of fields. Analysis of bio-samples including DNA, cancer markers, COVID-19 virus, bacteria are achieved by SERS technique [4-7]. Identification of food adulterants, environmental contaminants and narcotic drug analytes are also reported [8-11].

The remainder of this thesis is structured as follows.

Chapter 1 discusses theory, fundamental concepts, instrumentation, and applications of SERS. Electromagnetic enhancement, chemical enhancement, and evaluation criteria to judge an ideal SERS substrate is explained.

Chapter 2 starts with dedicated section to overview material processing by lasers, related absorption dynamics and adds to the foundations in the previous section to investigate formation of LIPSS on semiconductors. Existing models to explain formation of nanoripples are discussed.

Chapter 3 presents all experimental methods in this research.

Chapter 4 presents results of SERS measurements, micro-Raman mapping measurements, dark field scattering spectra. 3D COMSOL simulations allows comparison of experimental enhancement factors and theoretically calculated field enhancement values.

Chapter 5, the conclusion part will provide an outlook on obtained results, discussions and future studies.

Chapter 4 and 5 have used material from the following publication.

Erkızan, S. N., İdikut, F., Demirtaş, Ö., Goodarzi, A., Demir, A. K., Borra, M., Pavlov, I., & Bek, A. (2022). LIPSS for SERS: Metal Coated Direct Laser Written Periodic Nanostructures for Surface Enhanced Raman Spectroscopy. Advanced Optical Materials, 10(22), 2200233.

1.2   Light Matter Interaction and Raman Scattering

Relativistic and quantum theory of light has played a crucial role in understanding the interaction of electromagnetic radiation with matter. The interaction of photons with a molecule results some major optical phenomena such as photon absorption, photon scattering, emission, reflection, and transmission. Light scattering from matter varies due to inelastic and elastic collisions. Missing parts in the classical wave theory to explain light scattering contributed to the discovery of Raman scattering. C.V Raman focused on molecular diffraction of light by considering the light-quantum formulation of Einstein-Smuluchowski and tried to explain the relation between scattering power of medium and molecular structure. Theoretical prediction of Raman effect was presented by Adolf Smeakel in 1923 and discovered by C.V Raman in 1928 [12]. Discovery of the Raman effect paved the way for non-destructive vibrational spectroscopic technique and molecular physics that allows the identification of the molecular fingerprint of the substrate by specific molecular vibrational energy.

Raman scattering relies on the energy shift in lattice crystal or molecular vibrations due to inelastic scattering of incident radiation. Inelastic scattering of photon from lattice or molecular vibrations causes momentarily transition to virtual energy states. Due to conservation of energy, the frequency of scattered light is shifted. The Raman shift with scattered photon energy hν' demonstrated as,

$$\Delta v = \frac{1}{\lambda_{incident}} - \frac{1}{\lambda_{scattered}} \qquad\qquad 1.1$$

After the scattering, molecule may deliver its vibrational energy to the scattered photon and frequency of light is increased. This phenomenon is defined as Anti-Stokes shift. Reversely, for the Stokes shift, molecule may place in more highly excited vibrational state and the frequency of the shifted light is decreased. Scattering process without a change of frequency is defined as Rayleigh scattering. Jablonski energy diagram demonstrating electronic energy levels and vibrational energy levels of the molecule and related Anti-Stokes, Stokes and Rayleigh spectra are shown in Figure 1.1 and Figure 1.2 respectively.
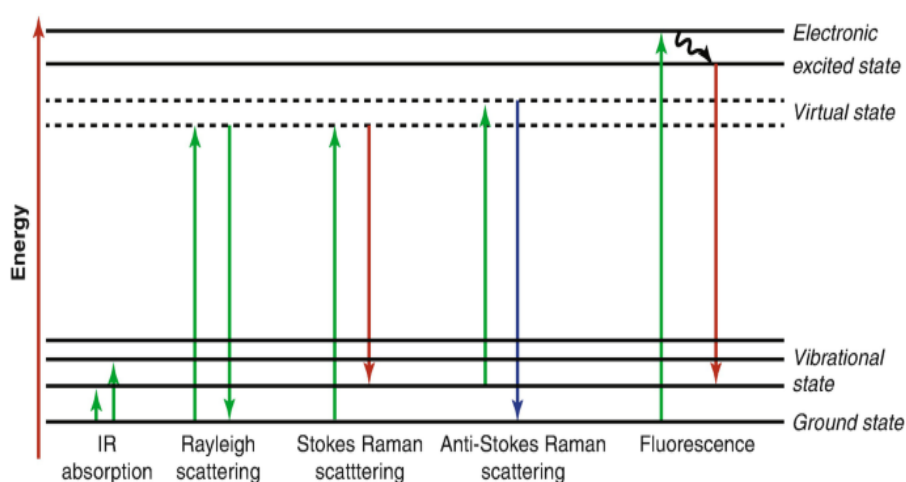
Figure 1.1 Jablonski diagram demonstrating electronic energy and vibrational energy levels of the molecule for different optical interactions.
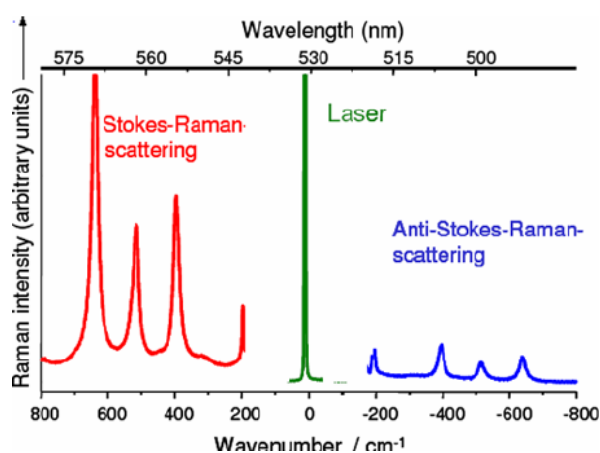
Figure 1.2 Illustration of typical Raman spectrum, Anti-Stokes (blue), Rayleigh (green) and Stokes (red) peaks.

According to the Maxwell- Boltzmann distribution demonstrated at Equation 1.2, the molecule population at the electronic ground state is much higher than the first excited state. Therefore, Stokes lines in the spectrum are observed much higher than Anti-Stokes lines due to relative high probability of thermal excitation. Because of that Stokes line are preferred in most cases even if symmetrically located Anti-Stoke lines deliver same information.

$$\frac{P_1}{P_2} = e^{-\Delta E/kT} \qquad\qquad 1.2$$

Explanation of the Raman scattering in the classical wave interpretation rather than quantum particle interpretation states that oscillating electric field E presence induces a dipole moment p, with proportionality constant a as a polarizability. Distortion tendency of an electron cloud due to presence of an oscillating electric field is defined as polarizability. It depends on bond length of the molecule, electron density and bond strength.

$$P = a\text{E} \qquad\qquad 1.3$$

$$P = aE_0\cos(2\pi vt) \qquad\qquad 1.4$$

$$P = aE_O(co\,s(2\pi vt) + \frac{1}{2}\,(\frac{\partial a}{\partial q})E_0[\cos(2\pi(v - v')t) + \cos\,(2\pi(v + v')t] \quad 1.5$$

In equation 1.5, the first term represents Rayleigh scattering, second term Stokes shift and third term Anti-Stokes shift. Polarizability of the molecule may not be identical in all applied E field directions. For the Rayleigh scattering, isotropic polarizability leads to radiation at the incident frequency. Anisotropic polarizability and dependence of vibrational and rotational coordinates can result in Raman scattering. Q is defined as normal coordinate of the vibration and Raman active modes exhibit a change in the polarizability α during the vibration, while IR active vibrations exhibit a change in dipole moment of the molecule μ,

$$\frac{\partial Q}{\partial \mu} \neq 0 \qquad\qquad 1.6$$

$$\frac{\partial Q}{\partial \alpha} \neq 0 \qquad\qquad 1.7$$

All molecule modes cannot be considered as Raman active modes except for the molecule that has no symmetry element. Rule of mutual exclusion states that for the centre of symmetry modes, IR active modes are Raman inactive modes.

Raman effect derivation can be performed by classical wave interpretation. Diatomic molecule can be considered as a classical harmonic oscillator that is given in Figure 1.3. Molecule bond strength-spring constant K and m-atomic mass analogy allows use of a Hooke's Law,
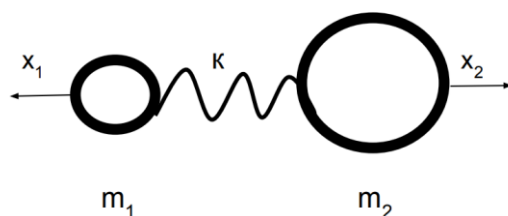
Figure 1.3 Harmonic oscillator to represent Raman effect of diatomic molecule by classical wave interpretation.

Presence of electric field leads to polarization of the molecule and harmonic variation imposed by nuclei on this polarizability. Different perturbations implied by nuclei, different polarizabilities and different frequencies are introduced. Raman scattering has inverse proportionality to the fourth power of the excitation wavelength. As a result, frequency of the diatomic molecule is written as,

$$\nu = \frac{1}{2\pi} \sqrt{\kappa \left(\frac{1}{m_1} + \frac{1}{m_2}\right)}$$ 1.8

Differential Raman cross section $\frac{d\sigma_r}{d\Omega}$ is defined to identify the amount of Raman scattered light by a randomly oriented molecule with respect to incident polarization. Differential Raman cross section that depends on Raman excitation wavelength, refractive index of ambient medium is defined for each vibrational mode.

Photon conversion into emitted Raman photons has inherent low probability and consequently low intensity Raman spectra are not detectable for studies. Besides, dominant fluorescence or poor signal to noise ratio can make Raman signal "invisible". Therefore, signal amplification techniques are required for many applications that demand good signal to noise ratio to improve capability to detect low concentrations. The field of SERS as highly sensitive and analytical technique for ultra-high signal amplification are discussed in the section 1.3.

1.3   Surface Enhanced Raman Spectroscopy (SERS)

Surface enhanced Raman spectroscopy (SERS) is a non-destructive, highly sensitive and label free vibrational spectroscopic technique that combines high field amplification aspect of plasmonic metal nanostructures with high molecular specificity of Raman spectroscopy [13]. This analytical technique for molecular identification discovered by Fleischman et al. in 1974 for a pyridine adsorbed at silver electrode and correct interpretation was presented by Van Duyne et. al [14]. Theoretical mechanisms and overall enhancement factor that are attributed to the

SERS effect includes electromagnetic enhancement (EM) mechanism and chemical enhancement (CE) mechanism. EM is based on excitation of Localized Surface Plasmon Resonance (LSPR) whereas CE is based on a charge transfer between analyte and metal particles and generally generates metal-molecule bonds to form charge-transfer complex. Orientation of the molecule relative to the surface normal is also crucial in SERS. Extremely high electric field enhancements in SERS are just observed in plasmonic gaps, *hot spots* where the electric field is highly localized. Hot spots are also observed at sharp edges and tips. Even though 10^6-10^{10} ranges for SERS enhancement were achieved experimentally, theoretical limit 10^{12} was assigned as a maximum EF range by Maxwell's equations [15]. Principles of the SERS mechanism for the Ag and Crystal Violet (CV) coated nanoripples are illustrated in the Figure 1.4.
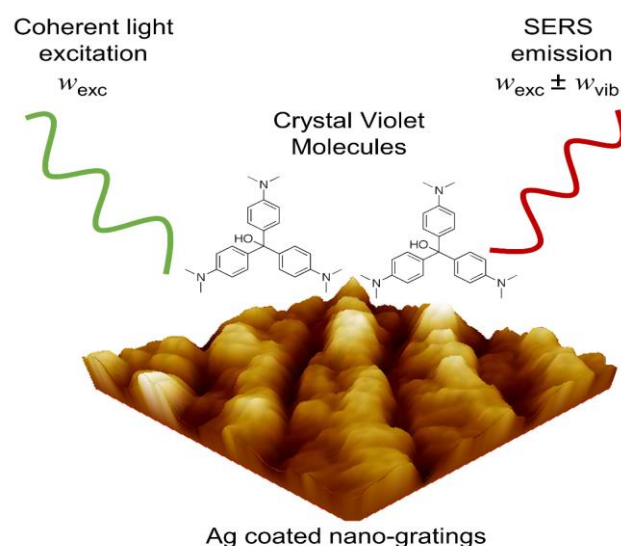
Figure 1.4 Schematic for SERS measurement of Ag coated femtosecond laser written substrates.

The field of SERS is recently undergoing a quite dynamic development and has applications in a wide variety of fields including single molecule detection, polymer science, spectro-electrochemistry, gas phase chemical detection, biosensing [16-19]. To reach ideal SERS substrates, recent strategies to generate highly sensitive SERS substrates focus on other evaluation criteria: spatially uniform EF, reproducibility,

8

precision, chemical stability, fast and low-cost fabrication in large areas with less contamination. SERS substrate generation techniques in the literature can be divided into three categories: metallic nanoparticles, nanostructured surfaces, and three-dimensional hybrid surfaces. The overview for three different SERS substrates with basic SERS substrate evaluation criterias are listed in Table 1.1.

Table 1.1 Comparison of commonly used and recent techniques to fabricate highly sensitive SERS substrates.

SERS Substrate	(EF)	LOD	Analyte	Pro	Application	Ref
Ag nanoparticle	2.7×10^7	10^{-8} M	R6G	stability	dye sensing	39
Au sphere monolayer	5.4×10^{10}	10^{-13} M	$C_{10}H_8S$	label free	bio-sensing	42
Ag nanoparticle on nanowire array (MACE)	1.4×10^8	10^{-9} M	R6G	robustness	bio-sensing (neurotransmitter)	55
Ag/ nanoparticle embedded LIPSS	1.5×10^8	10^{-9} M	MB	multiple utility, uniformity	dye sensing	96
Fs- generated micro-square arrays	1.2×10^{10}	10^{-11} M	MB	reproducible	dye sensing	97
Laser written Ag-Au deposited hallow fiber	1.0×10^5	10^{-7} M	R6G	3D SERS microcavity	dye sensing	98
Ag film on microfluid chip	not provided	10^{-15} M	CV	SMD, reusable	single molecule detection	-
3D Au dual rim-nanoframes	3.68×10^7	10^{-11} M	HCG	advanced synthesis strategy	biosensing (HCG)	56
TiO$_2$-Ag hybrid nanoarrays	7.95×10^5	10^{-9} M	CV	PIERS technique	dye sensing	32
Ag NPs on Si nanowire	1.6×10^6	10^{-11} M	RG6	3D hot-spot	dye sensing	53
Ag nanocubes	1.28×10^{10}	10^{-15} M	DNT	variety of detection	explosive-sensing	41
Ag nanowires	6.93×10^{13}	10^{-14} M	R6G	facile synthesis	sensing	40

Comprehensive review and comparison of all three types of SERS substrates, recent strategies to increase hot spot density and their state of art results in the literature will be provided in section 1.5. Advantages of the femtosecond laser-based techniques to fabricate highly sensitive SERS substrate will be underlined after we provide theoretical background about SERS phenomena.

1.3.1 Localized and Propagating Surface Plasmon Polaritons

Collective oscillations of conduction electrons are defined as plasmons, also called as quantum plasma oscillations. Coherent and collective electron oscillations at the interface between dielectric material and metal are called as surface plasmon. The term "polariton" defined by Fano in 1956 as a strong coupling of electromagnetic wave and plasmon [20]. Surface plasmon modes (the term "mode" describes an allowed state) can be divided into two categories: localized surface plasmon (LSP) and propagating surface plasmon (PSP). For the metal nanostructures, local confinement of electron oscillations on the metallic nanostructure's surface are called as LSPs. Metallic nanostructures that obey quasi-static limit (uniform electric field over the nanostructure), scattered photon from metallic nanostructures exhibit varying frequencies with different ambient media, intrinsic property, size and morphology. Plasmon excitations propagating at the boundaries defined as *surface plasmon polariton* (SPPs). Incident radiation with wave vector parallel to the surface are coupled with free electron gas. This configuration demonstrates propagating surface plasmon (PSP). Excitation of PSPs was presented in the literature by grating coupling and prism coupling [21-23]. Figure 1.5 and Figure 1.6 demonstrates LSPs and SPPs.
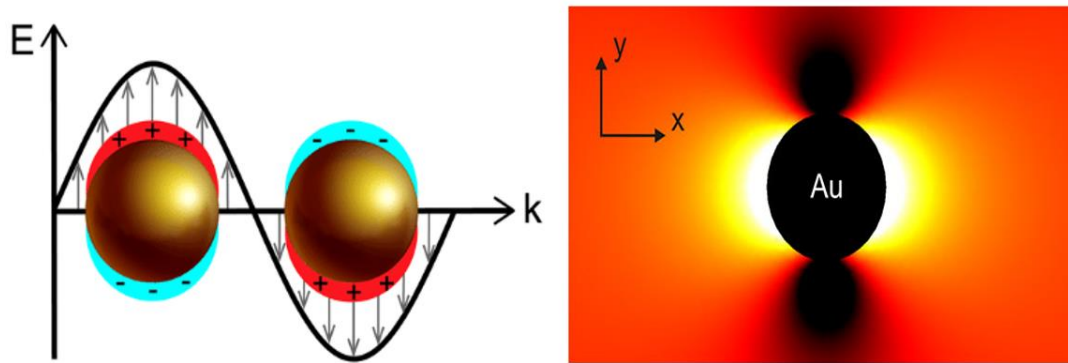
Figure 1.5 Representation for Localized Surface Plasmon of the Au nanospheres (LSP), (b) Theoretical electric field distribution of 20 nm Au nanoparticle for x polarized incident field at $\lambda = 522$ nm [24].
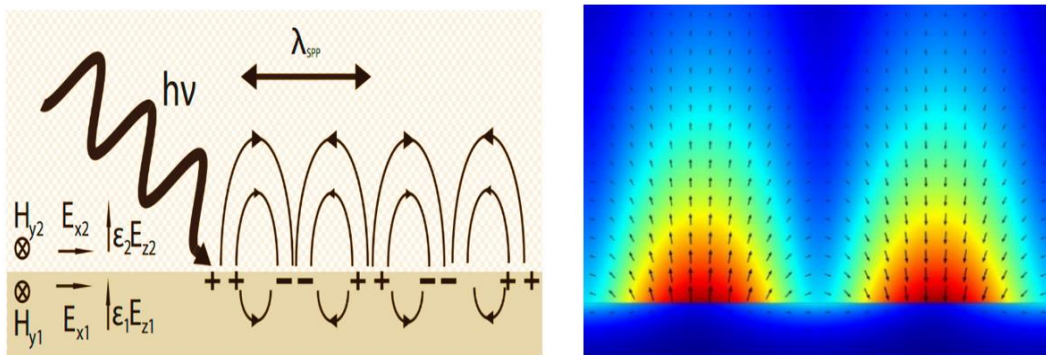
Figure 1.6 Representation for propagating Surface Plasmon Polariton (SPP) of the Au nanospheres (LSP), (b) Theoretical electric field distribution [25].

To derive plasmon frequency, plasma model is used. Equation of motion of the electron oscillations due to presence of applied electric field can be written as,

$$m\ddot{x} + m\gamma\dot{x} = -eE \qquad\qquad 1.9$$

Applied electric field,

$$E(t) = E_0 e^{-iwt} \qquad\qquad 1.10$$

$$x(t) = x_0 \, e^{-iwt} \qquad\qquad 1.11$$

Dislocated electrons affect overall polarization P,

$$P = -\frac{nE^2}{m(\omega^2 + i\gamma\omega)} E \qquad\qquad 1.12$$

Dielectric displacement D that equals to the $\varepsilon_o E + P$, is written as

$$D = \varepsilon_0 \left(1 - \frac{\omega_p^2}{\omega^2 + i\gamma\omega}\right) \qquad\qquad 1.13$$

Plasma frequency ω_p,

$$\omega_p^2 = \frac{ne^2}{\varepsilon_0 m} \qquad\qquad 1.14$$

Frequencies are restricted $\omega < \omega_p$ and for the large frequencies damping can be neglected.

$$\varepsilon(w) = 1 - \frac{\omega_p^2}{\omega^2} \qquad\qquad 1.15$$

Optical resonance conditions for metal structures have strong dependence on the size and shape of the metal, in addition to the intrinsic material properties of the metal. When we consider laser irradiated metallic sphere, simple and most intuitive approach would be electrostatic approximation since the size of the sphere is much smaller than the irradiation wavelength. Laplace's equations in spherical coordinates are solved with proper boundary conditions at radii to find electric field inside and outside of small metal sphere,

$$\frac{1}{r^2 \sin\theta} \left[\sin\theta \frac{\partial}{\partial r} \left(r^2 \frac{\partial}{\partial r} \right) + \frac{\partial}{\partial\theta} \left(\sin\theta \frac{\partial}{\partial\theta} \right) + \frac{1}{\sin\theta} \frac{\partial^2}{\partial\Phi^2} \right] \Phi\,(r, \theta, \Phi) = 0 \quad 1.16$$

From the axial symmetry,

$$\Phi_{inside}(r, \theta) = \sum_l^\infty A_l r^l P_l(\cos\theta) \qquad\qquad r < a \qquad 1.17$$

$$\Phi_{outside}(r, \theta) = \sum_l^\infty (B_l r^l + C_l r^{-l-1}) P_l(\cos\theta) \quad r > a \qquad 1.18$$

Applying boundary conditions properly,

$$\left.\frac{\Phi_{inside}}{\partial r}\right|_{r=a} = \left.\frac{\Phi_{inside}}{\partial r}\right|_{r=a} \qquad \text{1.19}$$

$$\varepsilon \left.\frac{\Phi_{inside}}{\partial \theta}\right|_{r=a} = \varepsilon_0 \left.\frac{\Phi_{inside}}{\partial \theta}\right|_{r=a} \qquad \text{1.20}$$

Gives electric field inside a small metal sphere as,

$$E_{inside} = \frac{3\varepsilon_m}{\varepsilon(\omega)+2\varepsilon_m} E_0 \qquad \text{1.21}$$

For the case which $\varepsilon\ (\omega)$ is approximately equals to the -2 ε_m, denominator goes to zero and the resonance condition is observed. Negative real part of the dielectric function can be associated with plasmon resonances. This example clarifies that proper plasmonic materials are required to have dielectric functions whose real part is small and negative while the imaginary part related with absorbance is small. This case is also an example of excitations which are confined to localities. They are defined as localized surface plasmon polariton (LSPs). Resonance conditions are called as Localizes Surface Plasmon Resonance (LSPR).

Randomly organized metallic nanoparticles do not exhibit specific phase relationships. However, when metallic nanoparticles are properly organized and distributed in a periodic array such that irradiation wavelength close to the period of the arrays, scattered field may be in phase with incident radiation. Such a reinforcement condition requires proper determination of periodic array, size, and morphology of the metallic nanoparticles. Consequently, LSPs coupled at a far field can greatly increase the quality factor of the resonance [26].

1.3.2 Plasmonic Enhancement and Localized Surface Plasmon Resonance (LSPR)

In the previous section, we have focused on coherent localized plasmon oscillations that result from interaction between the free electrons in a conduction band and the incident irradiation. Oscillating electric field with amplitude E_o and frequency ω_{inc} is introduced by incident laser irradiation drives plasmons in a nanomaterial. Resonance frequency of plasmons (ω_{max}) depends on ambient medium ε_{medium}, dielectric functions of the nanoparticle ε_{metal}, nanoparticle separation, size, and morphology of the nanoparticle. Resonant excitation of plasmons in a metal by electromagnetic wave results charge separation. This type of resonance is defined as Localized Surface Plasmon Resonance (LSPR).

Electric field strength $E_0(\omega)$, and polarizability of a metal sphere a_{metal} , determines magnitude of induced dipole $\mu_{induced(metal)}$,

$$E\ (\omega_{incident}) : \mu_{induced} = a_{metal}E_0(\omega) \qquad 1.22$$

Nanoscale Hertzian dipole is generated that emit radiation at the same frequency. Resonant inelastic light scattering of metal nanoparticle results local electric field enhancement $E_{local}(\omega_{inc})$ in the vicinity of nanoparticle and intense surface plasmon absorption bands are introduced. Introduced field $E_{local}(\omega_{inc})$ presence induce dipole for the molecule on the nanoparticle similar to induced dipole of metal nanoparticle.

$$\mu_{induced\ (molecule)} = a_{molecule}\ E_{local}(\omega_{inc}) \qquad 1.23$$

Light scattering can be demonstrated by $E_{local}(\omega_{inc})$ and vibrating molecule with eigenfrequency ω_{vib}. Dipole components expressed related with Anti-Stokes-Rayleigh and Stokes scatterings are listed respectively as,

$$[\ \mu_{ind}(\omega_{inc} + \omega_{vib}),\ \mu_{ind}(\omega_{inc}),\ \mu_{ind}(\omega_{ind} - \omega_{vib})] \qquad 1.24$$

Ag and Au are most frequently used nanoparticles in plasmonic applications. Resonance frequencies of colloidal Ag and Au are in the visible ranges needed to highlight since Raman excitations occur in these ranges [27]. Au and Ag have very similar electronic structures as their dielectric functions of these materials implies. Therefore, they exhibit similar optical properties.

1.3.3 Electromagnetic Enhancement and Chemical Enhancement

Overall SERS EF covers both EM and CE mechanism. Maximum efficiency of emission and excitation part of the Raman results maximum field enhancement. Theoretically, requirements of this condition can be satisfied for a substrate with a one plasmon resonance peak when the irradiation source is tuned to plasmon resonance peak [28].

Amplified electric fields are observed at *hot spots*. For the nanospheres, highest enhancement is recorded in the few nanometer distance to the substrate (Figure 1.7).

Raman enhancement includes both excitation and emission enhancements. Therefore, total SERS intensity related with electromagnetic enhancement expressed as both incoming and outgoing fields.

$$I_{SERS} = I_{inc}\,(\omega_{inc})I(\omega_{inc} - \omega_{vib}) \qquad 1.25$$

$$I_{SERS} = |E_{inc}(\omega_{inc})|^2|E_{inc}(\omega_{inc} - \omega_{vib})|^2 \qquad 1.26$$

In general, an approximation is used for fields in the blue region,

$$I_{SERS} \approx |E|^4 \qquad 1.27$$

Since the electric field dependence of distance expressed as,

$$E(r) = \frac{1}{r^3} \qquad 1.28$$

Distance dependence of SERS shown as,

$$I_{SERS} = \frac{1}{r^{12}}$$ 1.29
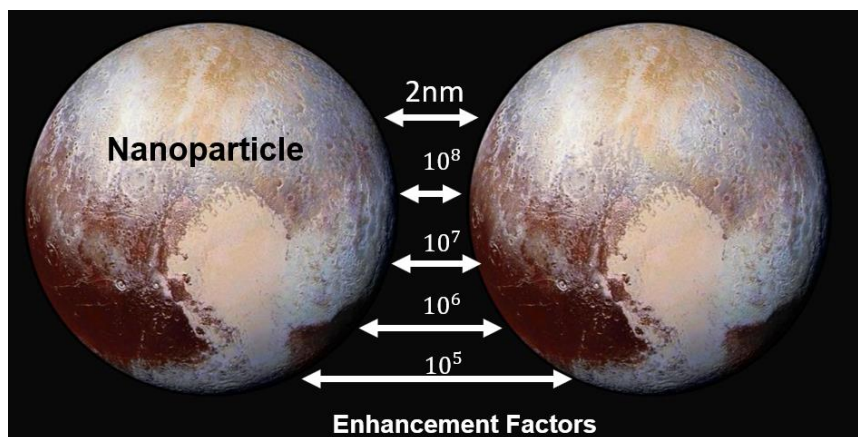
Figure 1.7 Order of enhancement factor dependence related with nanoparticle separation. *Hint for illustration: The term nano comes from Ancient Greek meaning "dwarf"*.

Electromagnetic field enhancement dominantly contributes to the overall SERS enhancement. Aforementioned field approximation holds for the cases where Raman shift is small compared to the frequency ranges where local fields exhibit profound changes. Electric field concentration increasing at sharp ends and tips is termed as lightning rod effect [29].

SERS as molecular spectroscopic technique intrinsically involves chemical enhancement mechanisms which arise due to metal- molecule interaction that is called as chemical enhancement (CE). Usual CE contributions to overall enhancement are typically reported in the range between $10 - 10^4$. As an extremely strengthened chemical enhancement, maximum contribution reported as 10^7 by Wang et. al [30] by manipulating heterojunction structure of the graphite carbon nitride and molybdenum disulphide nanoflower. Raman scattering cross section of

the molecule can be enlarged due to CE since electronic properties of adsorbate can change polarizability of the molecule [31]. Very recent strategy focusing on amplification of CE is called Photo Induced Enhanced Raman Spectroscopy (PIERS) [32]. PIERS technique includes plasmonic nanoparticle and metal oxide semiconductor interface. Oxygen vacancies are produced by UV laser irradiation. Later on, Raman excitation is applied and charge transfer from metal oxide to plasmonic nanoparticles is achieved [33].

Sites at different locations do not contribute equally to the exhibited SERS signal even for a uniform molecular distribution on the surface. Number of hot spots is extremely low. Hot spots represent 63 out of 10^6 sites. However, hotspot contribution   was reported as 24% [34].

1.3.4   SERS Uncertainty Principle

Simultaneous investigation of enhancement factor and substrate structure at the atomic scale was considered as an uncertainty case for SERS phenomena. This principle was defined by Natan in 2005, *Faraday's Discussions* [35]. High order of enhancements in the range $10^7 - 10^{10}$ observed more often in randomly located plasmonic substrates which geometrical parameter to obtain these structures are hard to control. This situation leads to inhomogeneous SERS signal distribution and more difficult characterization of hot spots and enhancement factor. Besides, when we demand higher field enhancements, the geometrical variables become more difficult to control experimentally. Therefore, high precision offered by femtosecond laser writing (will be discussed in Chapter 2) is worth to note.

1.4   Evaluation Criteria for SERS Substrates

Although high sensitivity and highly localized electric field regions are primarily demanded for SERS substrates; substrate to substrate reproducibility, spot to spot reproducibility, fabrication on large area through a cost-effective technique are

crucial for ideal SERS substrate generation. To achieve high sensitivity and low detection limit, spatial and spectral resolution of the spectrometer is also considered. Measurement parameters which affect SERS performance involve acquisition time, power, spot size, wavelength of Raman excitation. Analyte molecules also contribute when there is a metal-molecule interaction therefore scattering cross section, uniform distribution of molecule over a SERS substrate, molar mass of the analyte also affect SERS performance.

1.5   Review of Methods for Highly Sensitive SERS Substrate Generation

Comprehensive review and comparison of the aforementioned three types of highly sensitive SERS substrates (nanostructures, nanoparticles, hybrid three dimensional structured substrates) are presented in this section. Techniques of SERS substrate generation, and strategies to increase hotspot density are provided. We attempted to cover most active and state of art concepts of SERS including its major applications. Future studies of SERS, possible concepts and wide range of applications will be discussed. Besides the high sensitivity, substrate to substrate reproducibility, spot to spot reproducibility, fabrication on large area through a cost-effective technique are crucial for ideal SERS substrate generation.

Colloidal plasmonic nanoparticles are one the most employed substrates for SERS signal amplification [36-40]. Nanoparticles produced by wet chemistry techniques such as chemical reduction, photoreduction and laser ablation can offer significant increase of field enhancement as high as 10^{10} [41-42]. A major advantage that comes with NP SERS substrates that easy size and shape manipulation, and they are adoptable for various cases to excite localized surface plasmons on the nanoparticle. Controlled aggregation of plasmonic nanoparticles allows three-dimensional distribution of the hot spot region. However, since the controlled aggregation is a dynamic process of nanoparticles in a solution, exhibited SERS spectra profoundly depend on experimental conditions. Therefore, reproducibility of exhibited SERS spectra is considered as poor even if reproducibility of generating the same size and

shape nanoparticles is high. Additionally, chemical stability of these particles suffer from oxidation of nanoparticles and SERS substrate aging measurements reveals that high SERS performance is lost. Nanoparticle deposition can be performed on a wide range of surfaces and provides flexibility to obtain SERS substrates. However, long range uniformity of the NP SERS substrates is limited due to restriction of ordering the nanoparticles. To combat this case, self-assembled uniformly oriented nanoparticles are studied [43]. Nanostructured SERS substrate typically involves periodic arrays of nanohills, nanotips, nanospheres. Substrate generation can be performed by top-down generation techniques such as nanoimprint lithography, electron beam lithography, focused ion-beam lithography, nanosphere lithography [44-48]. High shape and size variance of synthesized NP-SERS substrates limits the correlation between LSPR and far field effects. Non-uniformities of NPs result in spectral fluctuations of the SERS signal. Top-down approaches present well defined and uniform plasmonic structures over large areas with high tunability of the geometries. Separation between plasmonic materials causes higher correlation between local field spectral dependence and extinction spectrum on the contrary of the agglomerated plasmonic NPs. Localized plasmon resonance in the visible and NIR range involves both far field effects and local field effects including SERS. Localized plasmon resonances can be manipulated at specific wavelengths by varying size, shape and interparticle gaps by top-down approaches. However, limitations of the top-down approaches are listed as multiple fabrication steps and high cost. Top-down generation techniques can be also combined with bottom-up methods such as thermal deposition, RF sputter coating, chemical vapor deposition [49-51]. Hybrid three dimensional SERS substrates focus on more efficient use of Raman excitation focal volume (Raman probe volume) by providing additional hotspot generation on the z-axis. By ultrafast laser processing, metal assisted chemical etching (MACE), reactive ion etching (RIE) [52,56] 3D hybrid SERS substrates can be fabricated. Formation of MACE based nanotips and nanocones intrinsically require the use of plasmonic materials. Plasmonic residues after the process can be used for one pot SERS substrate generation technique. Plasmonic

particle distribution on closely packed nanostructures can be used. Nevertheless, uniform SERS substrate generation over large areas is very limited compared to femtosecond laser-based SERS substrates. We also covered MACE technique in Section 4.13 as a short discussion and future study.

CHAPTER 2

LASER INDUCED PERIODIC SURFACE STRUCTURES (LIPSS)

2.1 Laser-Matter Interaction

Laser induced material processing relies on detailed consideration of absorption dynamics. Energy absorption into irradiated material by laser processing primarily involves free electron absorption that is consecutively delivered to the lattice by electron-phonon interactions. Diffusivity of electron subsystems can be considered as a postman for this delivery. Absorbed energy conversion into heat typically occurs on a time scale shorter than the laser pulse duration [57,60] and it includes electron-phonon interactions, electron hole recombinations, ionized vapor-electron interactions and excitation of conduction or valence band electrons. Spatial distribution of transferred energy by laser irradiation of matter is expressed by absorption coefficient α, reflectivity R, and incident intensity of source as,

$$I(z, t) = I_o(t) (1 - R) \exp(-\alpha z) \tag{2.1}$$

Thermal diffusion for varying laser pulse durations involves different electron-phonon coupling terms and different modellings [58,59]. Heat penetration depth δ_{th}, depends on specific laser pulse duration ζ_{laser}, density of the material ρ, heat conductivity λ_w , specific heat c_ρ can be approximated as,

$$\delta_{th} = \sqrt{\frac{\lambda_w \zeta_{laser}}{\rho c_\rho}} \tag{2.2}$$

When the laser pulse duration is less than the time needed for electron cooling, electron phonon coupling time is neglected and pulse decay occurs before heat

transfer into the lattice [60]. For such cases direct material evaporation can be observed without melting and high precision of laser processing is provided. Laser processed materials may exhibit phase changes (solid-vapor/ solid-liquid) that can be used in a variety of fields including machining, laser assisted spectroscopy, laser cutting, welding, deposition [61-64]. Laser processing of materials that do not exhibit phase changes (solid-solid) may involve semiconductor annealing, hardening, bending and shocking [65-68]. To achieve high accuracy during laser structuring, energy transfer in a period smaller than the characteristic lifetime for thermal diffusion is achieved with ultrashort laser pulse durations. Heat affected zones by laser scanning are reduced. High intensity laser pulse can initiate non-linear effects such as multi-photon absorption. Subsurface structuring is achieved by high electric field focused inside of a transparent material [69].

2.2   Laser Induced Periodic Surface Structuring (LIPSS)

The research activities in the field of Laser induced periodic surface structure (LIPSS) have been ongoing ever since its discovery by Birnbaum in 1965 [70]. Nowadays, 160 publications that are in the field of LIPSS annually appear in the scientific literature (web of science results for the "LIPSS" is presented in Figure 3.1). Most of these are related to the use of femtosecond laser pulses [71]. Shorter pulse durations provided by femtosecond lasers leads to decrease of detrimental heating. Also, to initiate non-linear multi photon absorption process higher peak power values are provided. Accurate control of processing with high flexibility, strong material adaptability, and fast nanoripple fabrication over large areas are provided by ultrafast laser writing techniques. Laser induced periodic surface structures (LIPSS), nanoripples, are generated on solid or liquid surfaces with the interference between incident laser beam and plasmon polariton wave [72]. Occurrence of LIPSS is controlled with irradiation wavelength λ, number of pulses applied to the irradiated spot (N), polarization direction, laser influence and ambient medium [73]. Without individual line production by ultrafast laser scanning,

22

simultaneous production of laser induced lines are observed for irradiated spot area. Matter re-organization models of LIPSS including self-organized models focus on this observation. However, electromagnetic models include the most accepted theory related with LIPSS, which is an *efficacy factor* theory. It is based on interactions of electromagnetic radiation with a microscopically rough surface [74]. LIPSS periods that are drastically smaller than irradiation wavelength named as nanoripples or high spatial frequency LIPSS (HSFL). Reif and her/his colleagues suggest that HSFL results from self-organization of the irradiated material [75]. Classical near wavelength sized LIPSS is strictly differentiated from HSFL and termed as low spatial frequency LIPSS (LSFL). Nano-pattern which is perpendicular to the laser polarization is called "normal", while nano-pattern parallel to laser polarization called as "anomalous" [76]. Anomalous structures are related with thermochemical oxidization. On the other hand, normal structures are associated with spatially modulated material removal (ablation). Well aligned LIPSS is generally generated after irradiation by multiple laser pulses. Rough surface is formed by first pulse and it promotes the coupling of energy for the next laser pulses. Grating like LIPSS pattern are likely to be observed during repetitive exposure. Feedback processes in LIPSS process are divided into two categories: Intra-pulse and inter-pulse effects. Inter-pulse effects consist of topographical, structural, chemical, incubation effects. Inter- pulse effects change the surface topography via ablation. Intra-pulse effects consist of stimulation of surface scattered electromagnetic wave (SEW) and excitation of transient defect states [77,78]. Even if the nature of LIPSS formation mechanisms require comprehensive models, existing models can be categorized as electromagnetic models and matter reorganization, self-organization models.
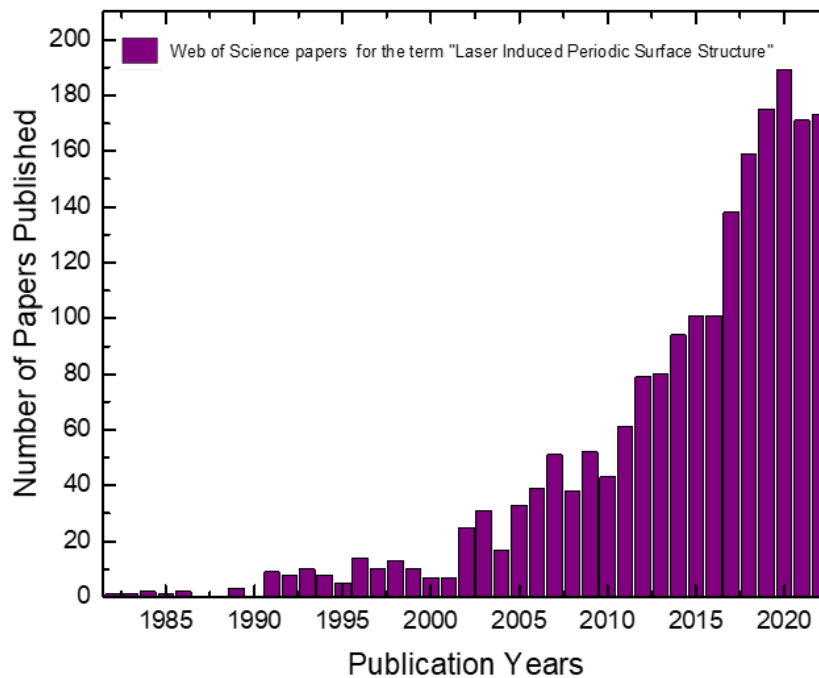
Figure 2.1 Web of Science results analysed in 04.12.2022 for the search term "laser induced periodic surface structure".

2.3 Electromagnetic Models for LIPSS

Electromagnetic models developed for LIPSS formation cover the most widely accepted LIPSS theory, which was presented by Sipe et.al in 1982 [74]. During ultrafast laser irradiation, scattered light at irregularities of the surface (scratches, defects, roughness, contaminants) may involve excitation of SPPs propagating along the irradiated surface. Even if LIPSS is a multi-pulse phenomenon, coupling of light to the SPPs is supported by initially ablated regions created with first laser pulses. Consequently, interference with electromagnetic radiation and SPPs imprint the laser fluence near the ablation threshold into irradiated material and selective ablation is observed. Different local fluence values and different number of consecutive pulses can result different periodicity regimes HSFL and LSFL on the same material [79,80]. Excitation of SPPs for plasmonically passive materials is achieved by irradiation with high intensity laser pulses and high number of free

carriers on the surface by profound dielectric permittivity changes and transition into metallic state $Re(\mathcal{E}) \leq 1$. Nonlinear multi-photon absorption mechanism is triggered by high intensity laser pulse exposure to the material. Inhomogeneous energy deposition into material is described by an efficacy factor function that defines varying LIPSS wave vectors as a function of surface roughness, dielectric permittivity, central wavelength, polarization direction, angle of incidence. Illustration for Sipe's theory for the LIPSS formation is given in Figure 2.2.
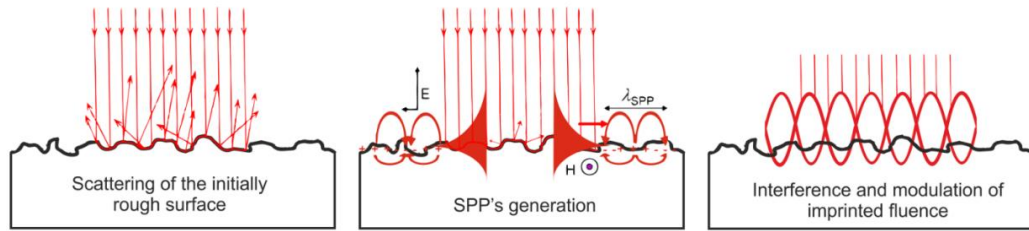
Figure 2.2 Schematic for Sipe's theory for the LIPSS formation.

2.3.1 Electromagnetic Absorption (Sipe's Theory) and Surface Scattered Electromagnetic Waves

By employing Green's formalism, dielectric polarization density at a microscopically rough surface is defined by Sipe's theory. The theory defines an efficacy factor $\eta(\mathbf{k}, \mathbf{k}')$ as a scalar function to describe surface roughness and dielectric permittivity dependent inhomogeneous energy absorption. Rather than analysing the LIPSS formation in real space, the process is studied in the Fourier domain spanned by wave vectors to cover prediction of LIPSS wave vectors as a function of surface roughness, dielectric permittivity and laser parameters. Scale of surface roughness in Fourier domain is defined by *b(k)*, and finally inhomogeneous energy absorption is expressed as,

$$\text{Absorption} = \eta(\mathbf{k}, \mathbf{k}').\, |b(k)| \tag{2.3}$$

Formation of LIPSS is typically presented for high efficacy factor differences. The b(k) transforms as the LIPSS is observed but this is the point where inter-pulse feedback mechanisms highly contributes. However, specifications for inter-pulse feedback mechanisms, laser parameters and template materials for LIPSS formation are not explicitly covered by Sipe's Theory.

2.3.2   Sipe-Drude Model

The extended theoretical approach combining efficacy factor theory and Drude model which describes optical response of laser irradiated material for further investigation of LIPSS mechanism is presented by Bonse et.al in 2009 [81]. Complex refractive index ń, number density N_e of quasi free electrons and non-linear Kerr effect are considered. Non-linear effects and specification for varying irradiation wavelengths and varying template materials are discussed. To clarify mandatory use of sub-picosecond pulse duration range for formation of HSFL structures are also analysed.

2.3.3   Feedback Mechanisms in LIPSS Formation

Feedback mechanisms in LIPSS formation consist of interpulse and intrapulse effects. Interpulse effect can be observed between multi-pulses, and intrapulse effect which can be related with even single laser pulse observed during initial stages of nanoripple formation. Self- organization, interaction with the ambient medium, incubation, chemical changes are related with *interpulse* effects while transitions into metallic states, optical constant changes, non-linear effects (*multi-photon absorption)* and surface plasmon generation are related with *intra-pulse effects*.

2.4   Matter Reorganization Models

We previously underlined another mechanism for formation of periodic nanoarrays which do not present laser induced patterns as a result of line-by-line laser scanning and nanoripple periodicities are far smaller than spot size of the laser beam, which hints towards self-organized LIPSS formation as a result of homogeneous irradiation. Hence, we separately discuss the matter reorganization models for LIPSS formation including self-organized models, hydrodynamic theories and material instabilities. The minimum energy density required for gradual material removal (ablation) is defined as the ablation threshold and it varies due to unique hydrodynamic mechanisms observed for different central wavelengths, pulse durations, irradiated template materials and pulse densities (the number of pulses on the irradiated spot). Local laser fluence values that are higher than ablation threshold causes the formation of LIPSS. Nanoripples formed perpendicularly to the laser electric field polarization vector. Non-linear heat exposed to the conduction band electrons are responsible for different hydrodynamic effects and it determines the different regimes for the gradual material removal [82,83]. For the modest fluence values which are slightly above the ablation threshold, gradual material removal rate is weakly introduced, and low rated evaporation of material occurs. For the fluence values strictly above the ablation threshold, gradual material removal rate is determined by heat penetration depth depending on electron heat diffusion length [84].
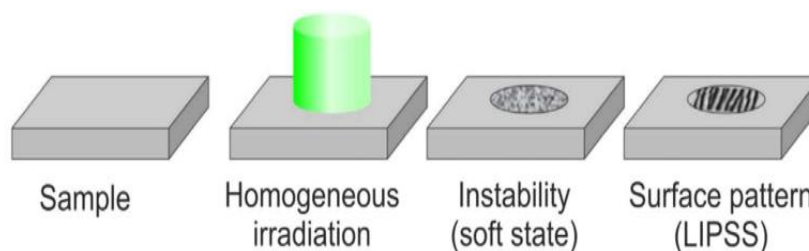
Figure 2.3 Illustration of matter reorganization models for formation of LIPSS patterns [85].

2.5 Low Spatial Frequency LIPSS (LSFL)

We previously stated that interference of the generated SPPs and incident laser irradiation forms LIPSS nanostructures and high intensity laser pulses are especially crucial for plasmonically passive materials to achieve transient change into metallic state. For the semiconductors and metals, LSFL structures with an orientation perpendicular to the beam polarization are called "normal". Formation mechanism of the normal structures are linked with gradual material removal (ablation) [76,86] Their periodicities are highly correlated with laser irradiation wavelength and SPP's wavelength. For the large band gap materials or dielectrics specific electromagnetic modes are introduced and periodicities of the nanoripples are correlated with $\frac{\lambda}{n}$. For these structures beam polarization is typically parallel to the orientation, and they are called "anomalous". Formation mechanism of anomalous structures is explained with thermochemical oxidization [87]. Interference of the far field scattered light and incident laser beam is considered.

2.6 High Spatial Frequency LIPSS

Sub-wavelength nanoripples with the periodicity smaller than half of the wavelength are called as HSFL structures. Generation of surface scattered second harmonics, sub SPPs, are proposed for the HSFL formation in the literature. Transition to the HSFL structures from LSFL structures can be observed on the same materials with varying fluence values and number of pulses [79,80].

CHAPTER 3

EXPERIMENTAL SECTION

3.1   Piranha and RCA 2 Wet Chemical Cleaning

Since we claim to obtain highly sensitive surfaces it would be very risky to keep possible unknown compounds on the surface, especially for the low CV concentration Raman measurements. Therefore, piranha and RCA wet chemical cleaning procedures are performed respectively to eliminate possible contributions of any other compound on the surface during Raman measurements. Besides, to perform uniform Ag deposition as much as possible on the the Si-LSFL and Si-HSFL substrates, wet chemical cleaning procedures are required. Cleaning procedures are not prerequisites for formation of Si-LSFL and Si-HSFL.

Si wafers, n-type Si Si <100> wafer (Czochralski, double-side polish, 275 µm, 1-3 Ω cm) is used as the processed material. All Si wafers are first exposed to piranha solution, 1:3 ratio of hydrogen peroxide (H_2O_2, Merck, 30%) and sulfuric acid (H_2SO_4, Merck, 95-97%) at 75 °C for 15 minutes. They are rinsed in deionized water. Later on, they are dipped into RCA solution 1:1:5 ratio of H_2O_2, hydrochloric acid (HCl, Merck, 37%) and water (H_2O), at 75 °C for 15 minutes. They are rinsed in deionized water for a while and dried by N_2 blowing. Moreover, Ti coated microscope slides are used as a processing template for Ti-LSFL formation. Before the Ti deposition on microscope slides, they are cleaned with piranha wet chemical cleaning procedure.

3.2   Formation of Si-LSFL and Ti-LSFL Structures

Si-LSFL formation is achieved by a homemade femtosecond laser operating at central wavelength 1032 nm, with spot size 16 µm, repetition rate 1 MHz, pulse

duration 370 fs. Ambient medium during the processing is air. The polarization is 45° with respect to scanning lines. By using a galvo scanner, periodic nanoripples are obtained in 5 mm x 5 mm area. Half wave plates and polarizers are used to control power and polarization. The polarization is 45^0 with respect to scanning lines. Controllable parameters are listed as pulse density, pulse energy and polarization direction of monochromatic light with respect to the scanning lines. Laser fluence for the Li-LSFL formation is 0.577 J/cm^2, while pulse energy is 1.2 µJ. Average pulses per focal spot are varied by different laser processing speeds. Different processing speeds 3, 5, 7 and 10 m/s which are related with number of pulses per focal spot 19.0, 11.5, 8,2, 5.7 respectively are tested to vary nano roughness created on Si.

The Ti-LSFL structures are fabricated on 350 nm Ti deposited microscope slide with 4 µm line/hatch distance with 12.5 pulse density (average number of pulses per area) and varying pulse energy from 0.75 µj to 1.2 µj. The polarization is 45° with respect to scanning lines.

3.3   Formation of Si-HSFL Structures

Si-HSFL formation is achieved by femtosecond laser operating at central wavelength 1550 nm, repetition rate 1 MHz, pulse duration 450 fs. To initiate two photon absorption phenomena during laser processing, laser fluence is adjusted as 2600 J/cm^2. HSFL nanoripples are obtained in 1 mm x 3 mm area. Reproducibility of the generated nanoripples are profoundly affected by focal depth. Polycrystalline Si is formed due to energy transfer into the material during laser scanning which results melting and recrystallization. Sub-surface structuring is revealed after removal of polycrystalline Si layer by dipping processed Si substrate into selective etchant [88].

3.4   Thermal Evaporation and RF Sputtering

Ag deposition on Si-HSFL and Si-LSFL substrates is performed by thermal and RF sputtering combined vacuum chambers, Nanovak NVTS-400. Ag is thermally evaporated on Si nanoripples while Ti deposition on microscope slides is performed by RF Sputtering. Chamber vacuum pressure, chamber temperature, deposition rate are kept same for each SERS substrate generation.

3.5   Scanning Electron Microscope (SEM) and Atomic Force Microscope (AFM) Imaging

SEM imaging is performed by FEI Quanta 400F Field Emission SEM (resolution 1.2 nm) and SEM images are used to analyse periodicity of the nanoripples. AFM imaging is performed by (Veeco - Multimode & Nanomagnetics Instruments - Ambient) to observe depths of the nanoripples. Additional sample preparation techniques are not used.

3.6   SERS Substrate Preparation

To achieve homogeneous molecule deposition on the SERS substrates and to avoid coffee ring effect, 100 µl of Crystal Violet ($C_{25}H_{30}ClN_3$, Sigma Aldrich) are spin coated (acceleration time 5 seconds, spanning time 30 seconds at 2000 rpm, deceleration time 3 seconds) onto Ag coated Si-LSFL and Si-HSFL substrates. Varying concentrations of CV molecules are spin coated (10^{-5}-10^{-10}) during limit of detection analysis of the SERS substrates. After CV deposition, SERS substrates are dried on hot plate at 30 $^{\circ}$C for 25 minutes.

3.7   SERS Measurements

Three different Raman excitation from linearly polarized continuous wave (CW) 532 nm, 660 nm and 785 nm wavelength laser sources are coupled to multimode (MM) fiber and passed through a modified upright microscope (Nikon Eclipse LV100) that involves 100X/0.90 NA objective. Schematic of the Raman setup is presented in Figure 3.1. For all Raman excitation wavelengths, same excitation powers 40mW (6.4 mW) are applied on the sample surface. The incident polarizations of the originally linearly polarized excitation lasers are scrambled due to MM fiber delivery. The Raman signal are collected in epi-configuration by the same objective lens and coupled into another multimode fiber through suitable dichroic mirrors (Semrock) and notch filters (Semrock). The characterization the Raman signal is achieved by a f/9.8, 750 mm spectrometer (Andor Shamrock SR750) with 150 l/mm grating and an EMCCD camera (Andor Newton).
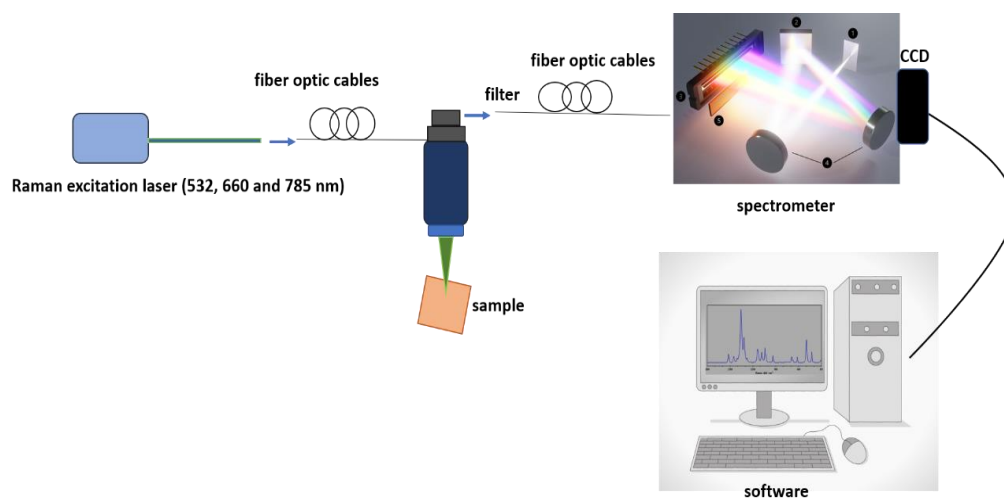
Figure 3.1 Schematic of the Raman setup. Three different Raman excitation wavelengths (532, 660 and 785 nm) are coupled into fiber optics and delivered to the Raman microscope and focused onto the SERS substrate to characterize frequency shifts via spectrometer and software. Rayleigh scatterings are excluded by notch filter.

3.8   Reflection Measurements

Calibration part of the reflection measurements are performed by locating $BaSO_4$ calibrating disk at the reflection port of the integrating sphere. $BaSO_4$ is preferred due to its high reflectivity within visible range and its flat spectral reflection response for UV-NIR wavelength range. Specular reflection port is kept closed during the calibration and reflection measurements. Wavelength of the light is adjusted in the visible range to check the position of the light beam on the calibration disk. Cover on the specular port is removed temporarily and the prism is located at the specular port to check beam alignment. Ag coated Si-HSFL and Si-LSFL structures with varying thickness are mounted the reflection port of the integrating sphere respectively and reflection spectra between 400-1100 nm are collected. Reflection set-up is presented in Figure 3.2. Spectral responsivity of the SERS substrates is investigated by monochromator and detector.
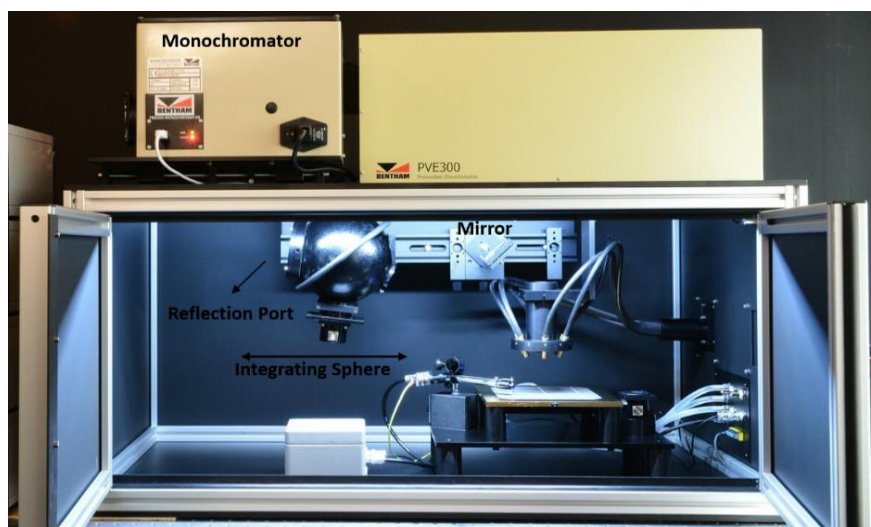
Figure 3.2 Bentham PV300 reflection set-up that involves reflection port at the left-hand side of the integrating sphere, monochromator, mirror and a light source.

3.9   Raman Mapping Analysis

N-phenyl stretching band of CV (peak located at 1374 cm^{-1}, peak width 1319-1421) is used for all analysis at 532, 633, and   785   nm   excitation   wavelengths (Renishaw/In   Via). Coordinate dependent spectra are collected to determine signal variance. Calculation is performed after normalization of raw spectral data and baseline correction. Plotting is achieved by data conversion into a matrix. Distance between acquisition points on the substrates are approximately   in 20 µm x 20 µm area. Batch processing in Origin is used to evaluate CV peak in all results. Peak width is considered to check fitting. Unreasonable fittings are removed with average of their localities.

3.10   Dark Field Microscopy and Dark Field Scattering Spectra

An inverted microscope (Zeiss - Axio Observer A1m) is utilized in dark-field reflection mode using corresponding dark-field objective and reflector modules (Zeiss) for both the optical examination and the scattering spectroscopy of the SERS substrates. Scattering spectra of the 70 nm Ag coated HSFL and LSFL structures are measured through the side port of the microscope with external optics through a miniature spectrometer (Maya 2000 Pro) and using a halogen light source (Zeiss - HAL 100).

3.11   Field Enhancement Simulations

Finite Element Method (FEM) based Maxwell solver simulations (COMSOL Multiphysics) are used for simulated enhancement factor results. To achieve most realistic representation of the SERS substrates SEM images are used. Randomly chosen 1.0 µm x 1.0 µm areas are represented. To emphasize hot spots and regions observed the lightning rod effect, colour map maxima is chosen as 14 in the logarithmic scale. Refractive index value is taken from Johnson and Christy.

CHAPTER 4

METAL COATED DIRECT LASER WRITTEN PERIODIC NANOSTRUCTURES FOR SURFACE ENHANCED RAMAN SPECTROSCOPY (SERS)

4.1   Introduction

Quasi periodic, self-organized laser written periodic nanostructures can embody required plasmonic gap distance, roughness and randomness to accommodate high hotspot density for SERS applications. Femtosecond laser written quasi-periodic nanostructures are generated in two different periodicity regimes, namely HSFL and LSFL. Accurate, flexible control of the processed region is provided by ultrafast laser writing compared to well established tow down approaches such as nanoimprint lithography, electron beam lithography. Nanoplasmonic SERS substrate generation is achieved by metal deposition onto HSFL and LSFL patterned Si. Profound localized field enhancement is introduced with silver coated nanoripples and overall EF reported as 10^9 that is comparable to most currently employed SERS substrates such as aggregated nanoparticle colloids, plasmonic nanostructures and hybrid SERS substrates. In addition to the high and spatial field amplification, chemical stability, robustness, fast and low-cost generation of SERS substrates are presented by femtosecond laser-based techniques. Schematic illustration for Si-LSFL and Si-HSFL SERS substrate generation and SERS measurement are shown in Figure 4.1.
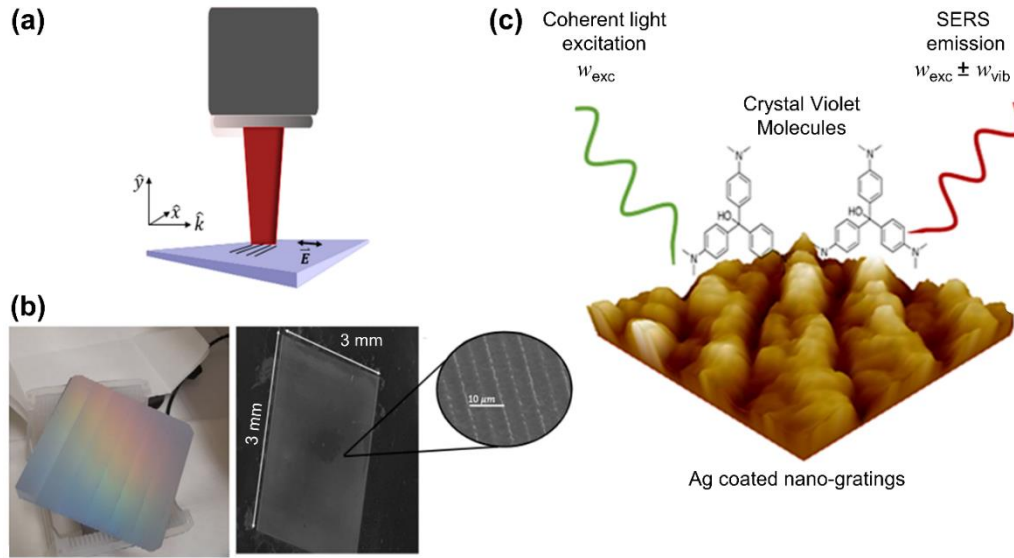
Figure 4.1 Overview of the SERS substrate generation by ultrafast laser writing technique (a), Si-LSFL pattern produced on a full Si wafer 6 cm x 6 cm and Si-HSFL pattern with dimensions 3 mm x 3 mm (c) Illustration of SERS measurement for ultrafast laser written nanostructures.

4.2 Direct Ultrafast Laser Writing for formation of Si-LSFL, Si-HSFL, Ti-LSFL Substrates

Femtosecond laser written quasi-periodic nanoripples can be categorized in terms of their periodicities as LSFL and HSFL LIPSS. Formation of nanoripples on Si can be controlled by irradiation wavelength, scanning speed, laser fluence, the number of pulses on spot, polarization direction of the beam, repetition rate. Si-LSFL formation is achieved by a femtosecond laser operating at central wavelength 1032 nm, with spot size 16 µm, repetition rate 1 MHz, pulse duration 370 fs. Laser fluence for the Si-LSFL formation is reported as 0.577 J/cm^2, while pulse energy is reported as 1.2 µJ. Pulses per focal spot are varied by different laser processing speeds. Si-HSFL formation is achieved by another femtosecond laser operating at central wavelength 1550 nm, repetition rate 1 MHz, pulse duration 450 fs. To initiate two photon

absorption phenomena during laser processing, laser fluence is adjusted as 2600 J/cm^2. Scanning Electron Microscope (SEM) images illustrating shape and size variation of both Si-HSFL and Si-LSFL structures after 30 nm Ag deposition and Raman dye deposition (Crystal Violet, 10^{-5} are presented in Figure 5.2. Continuous nanoripple formation is achieved over large areas with an orientation perpendicular to the laser polarization direction. Periodicities of LSFL nanoripples which have correlation between Surface Plasmon Polariton (SPP) wavelength are reported as 890 nm by calculating 2D-FFT (two-dimensional fast Fourier transform) of the structures. Depth of the Si-LSFL nanowells are averaged from AFM cross sections and reported as 390 nm. Sub-surface plasmon polaritons (sub-SPPs) generated at the subsurface of the materials have been suggested to explain formation of HSFL structures [89]. For the Si-HSFL structures two types of periodicities are introduced. Smaller periodicity of the features is determined as 290 nm by 2D-FFT calculations. Li.Z. et al. stated that competition between penetration loss of femtosecond laser pulse and propagation loss results the period of the HSFL structures. Depth of the Si-LSFL nanowells are averaged from AFM cross sections and reported as 105 nm. SEM images of the HSFL and LSFL structures are demonstrated in Figure 4.2 and Figure 4.3, while AFM images are given in Figure 4.4. Bigger periodicities observed for Si-HSFL structures are related with the 5 μm hatch distance.
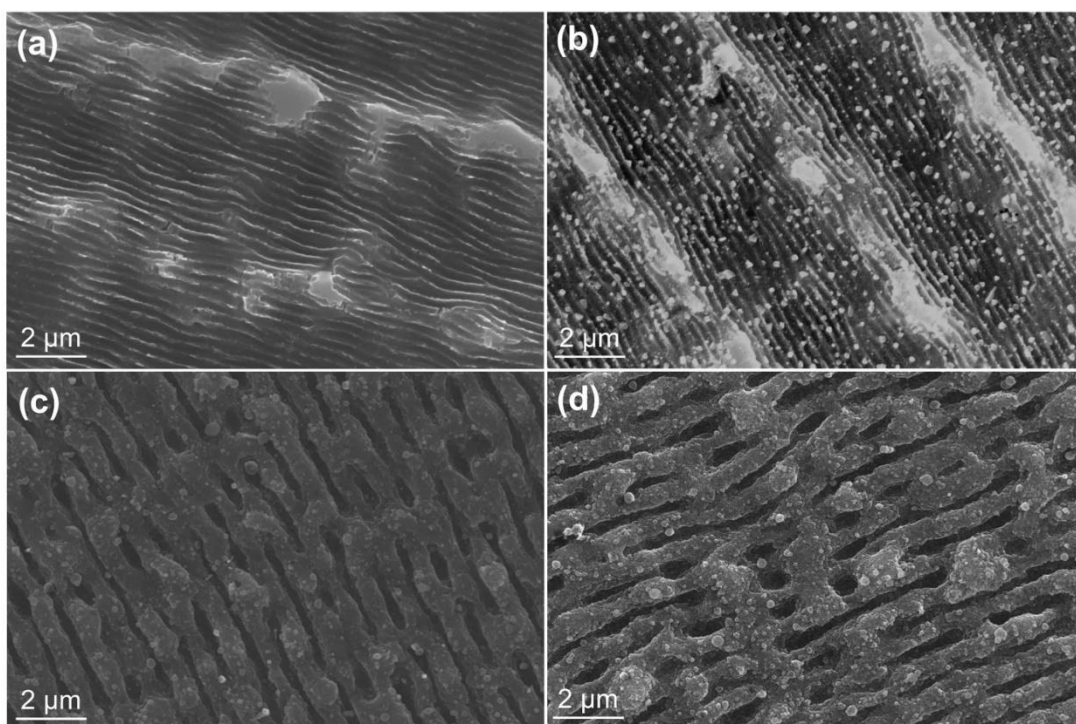
Figure 4.2 SEM image of (a) bare Si-HSFL produced by femtosecond laser, 30 nm Ag and 10^{-5} M CV coated Si-HSFL (b), bare Si-LSFL produced by femtosecond laser (c), 30 nm Ag and 10^{-5} M CV coated Si-LSFL (d).

Reducing plasmonic gaps of the nanoripples allows higher EF results by increasing hot spot density. Hence, we expect to observe quite different EF results for Si-LSFL and Si-HSFL structures due to their periodicities. SEM images with 10^5 magnifications in Figure 4.3 can be analysed further when we present comparable SERS EF results of Si-HSFL and Si-LSFL structures. We can state that irregular clusters observed on the Si-LSFL structures make an additional volume contribution for hot spot generation and competition is possible even for the Si-HSFL structures with smaller periodicities.
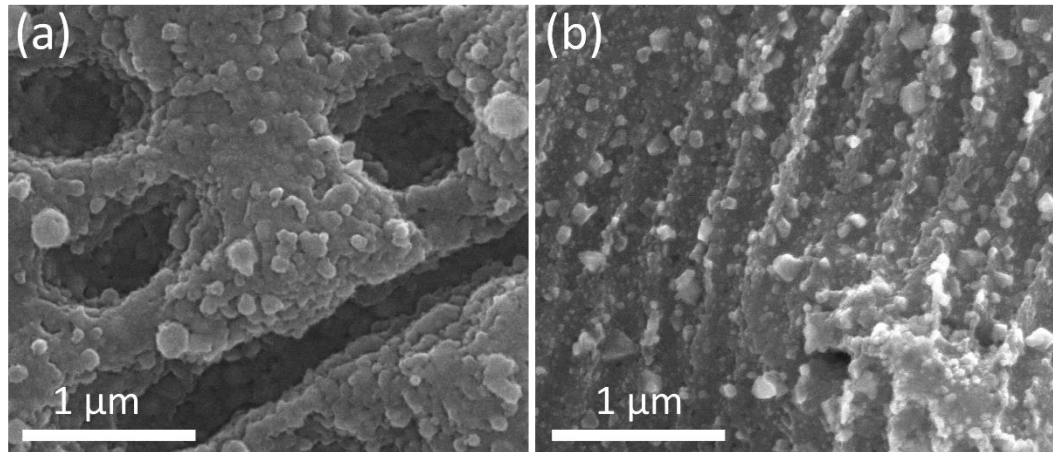
Figure 4.3 SEM image of Si-LSFL structure (a), Si-HSFL structure (b). Note the different magnifications with respect to previous SEM images.
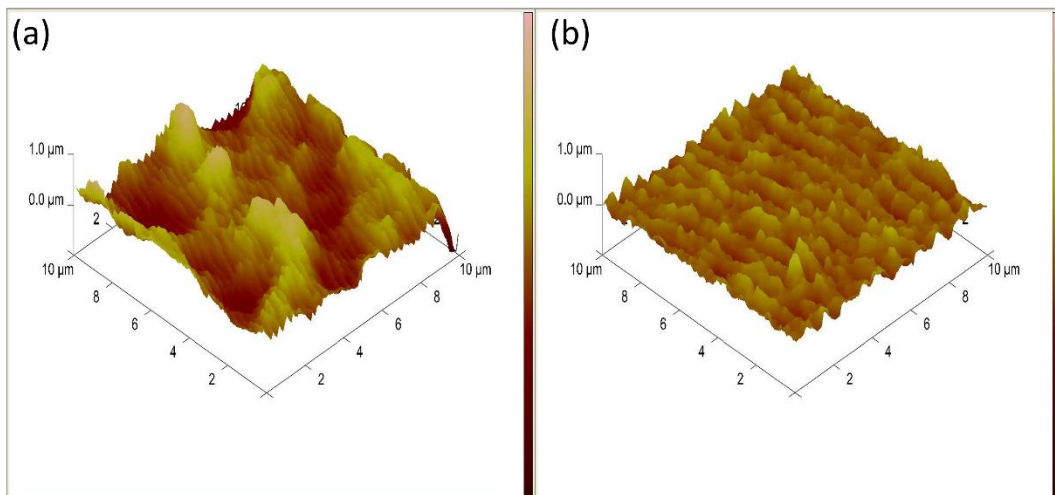
Figure 4.4 AFM images of Si-HSFL (a), and Si-LSFL (b) structures in 10 µm x 10 µm areas.

4.3   Ag Thickness Optimizations for Si-LSFL and Si-HSFL Substrates for Different Raman Excitation Wavelengths

To obtain highly localized field enhancement without losing increased nanoscale surface area achieved by femtosecond laser writing, thin film deposition thickness is

optimized for both Si-LSFL and Si-HSFL at 532, 660, 785 nm Raman excitation wavelength (Figure 4.5 & Figure 4.6). To avoid separate and non-uniform Ag cluster formation on the nanoripples, threshold thickness of uniform metal deposition determined as 40 nm for both Si-LSFL and Si-HSFL. To achieve the same thin film property on each SERS substrate deposition rate, angle of deposition, temperature of the chamber, high vacuum pressure are kept the same for each SERS substrate. Highest SERS signal range is observed for 70 nm Ag coated Si-HSFL structure at 660 nm Raman excitation wavelength. Optimized thin film depositions exhibit highest enhancement for different Raman excitation wavelengths 532, 660 and 785 nm.
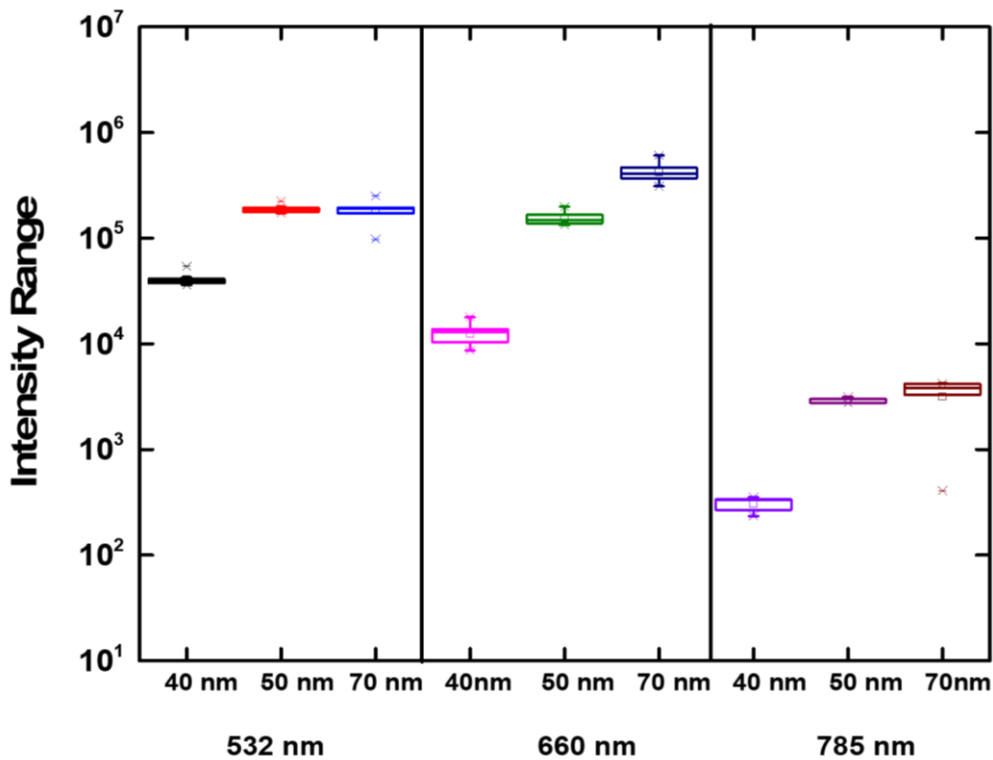
Figure 4.5 Box charts of Si-HSFL structures with varying Ag thickness; 10^{-5} M for different Raman excitation wavelengths respectively 532 nm, 660 nm and 785 nm. Each box chart displaying SERS intensity range for Si-LSFL structures represents collection of 20 measurements. For each Si-LSFL substrate, measurements are collected from five different locations, and Si-LSFL substrates generated with 4

different processing speed. We would like to underline that we do not share laser processing speed dependent intensity range but we present collection of all four processing speeds.
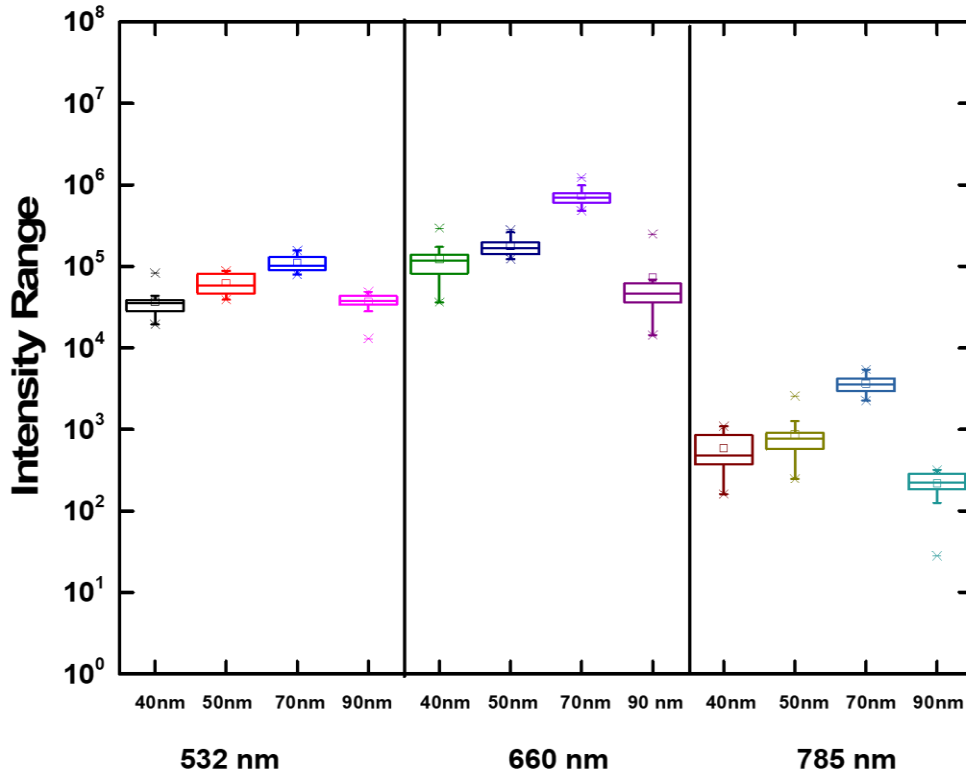
Figure 4.6 Box charts of Si-LSFL structures with varying Ag thickness; 10^{-5} M CV; for different Raman excitation wavelengths respectively 532 nm, 660 nm and 785 nm.

4.4 Enhancement Factor Results of Ag Coated Si-LSFL and Si-HSFL Substrates

Enhancement factor calculations are performed by the most applied approach used in the literature [90].

$$EF = \frac{I_{SERS}}{I_{Raman}} \text{ x } \frac{N_{Raman}}{N_{SERS}}$$ (4.1)

To calculate total number of molecules in the Raman measurement N_{Raman}, three-dimensional Raman probe volume for different Raman excitations is calculated. Prolate spheroid focal volume can be used to calculate three-dimensional Raman probe volume for 532 nm, 660 nm and 785 nm Raman excitation source. Even if spot size is a factor contributes simultaneously the numerator and denominator of surface averaged SERS EF calculations, laser spot size is considered separately for 660 nm and 785 nm EF calculation. For 532 nm excitation source prolate spheroid has dimensions $r_x = 8.5 \ \mu m$, $r_y = 8.5 \ \mu m$ and as a depth of focus $r_z = 17 \ \mu m$. Volume of the Raman probe V_{Probe}, is calculated as 5×10^{-12} L. N_{Raman} is calculated as 3×10^{10} molecules by considering Raman probe volume and C_{raman} for 10^{-2} M CV concentration,

$$N_{Raman} = C_{Raman} \times V_{Probe} \tag{4.2}$$

$$N_{Raman} = 10^{-2} \frac{mol}{L} \times 6.02 \times 10^{23} \frac{molecules}{mol} \times 5.10^{-12} L \tag{4.3}$$

For 660 and 785 nm Raman excitation source, N_{Raman} values are calculated as 5.8×10^{10} and 9.6×10^{10} molecules respectively.

I_{Raman} and I_{SERS} values for different Raman excitation wavelengths are calculated by measured area under the N-phenyl stretching band of CV (peak located at 1374 cm^{-1}, peak width 1319-1421). Calculation is performed after normalization of raw spectral data and baseline correction. To report probe volume of Si-LSFL structures $V_{Probe-LSFL}$ in the near field span up to 2 nm, surface area of the Si-LSFL substrate obtained from AFM images (10 μm x 10 μm area) are used. $V_{Probe-LSFL}$ is calculated as,

$$V_{Probe-LSFL} = 328.0 \ \mu m^2 \times 0.002 \ \mu m \cong 7 \times 10^{-16} \ L \tag{4.4}$$

Probe volume of Si-HSFL calculated through same strategy for obtained surface area 322.8 μm^2,

$$V_{Probe-HSFL} = 322.8 \ \mu m^2 \times 0.002 \ \mu m \cong 6 \times 10^{-16} \ L \tag{4.5}$$

Total number of molecules involved in the SERS measurements N_{SERS} are found both for Si-HSFL and Si-LSFL substrates at 532 nm Raman excitation wavelength,

$$N_{SERS-HSFL} = 10^{-5} \frac{mol}{L} \text{ x } 6.02 \text{x } 10^{23} \frac{molecules}{mol} \text{ x } 6 \text{x} 10^{-16} \text{ L} = 3.9 \text{ x } 10^3 \qquad (4.6)$$

$$N_{SERS-LSFL} = 10^{-5} \frac{mol}{L} \text{ x } 6.02 \text{x } 10^{23} \frac{molecules}{mol} \text{ x } 7 \text{x} 10^{-16} L = 4.2 \text{ x } 10^3 \qquad (4.7)$$

By applying same procedure, N_{SERS} values at 660 nm Raman excitation wavelength are reported as 5.9×10^3 for Si-HSFL and 6.0×10^3 molecules for Si-LSFL. For 785 nm excitation wavelength N_{SERS} values are reported as 8.4×10^3 for Si-HSFL, and 8.5×10^3 molecules for Si-LSFL. As a result, EF results of 70 nm Ag coated Si-HSFL and Si-LSFL substrates are obtained at 532, 660 and 785 nm (Table 4.1).

Table 4.1 Enhancement Factor results of 70 nm Ag coated Si-LSFL and Si-HSFL structures at different Raman excitation wavelengths.

Raman excitation (nm)	532	660	785
Si-LSFL	$1.7 \text{x } 10^8$	$1.6 \text{ x } 10^9$	$1.0 \text{ x } 10^7$
Si-HSFL	$5.8 \text{ x } 10^8$	$1.9 \text{ x } 10^9$	$1.8 \text{ x } 10^7$

Figure 4.7 represents enhancement factor distribution of Si-LSFL and Si- HSFL substrates at 532, 660 and 785 nm Raman excitation wavelength for varying Ag thin film thickness. Highest enhancement factors are reported as 70 nm Ag coated Si-LSFL and Si-HSFL substrates meaured at 660 nm excitation wavelength. SERS performance of 90 nm Ag coated Si-LSFL structures exhibit drastic decrease due to decreased surface area and hot spot density. Since average depth of the LSFL nanowells ($\cong 390 \ nm$) are much higher than average depth of HSFL nanowells ($\cong 105 \ nm$) it is quite natural to observe gradually planarized Ag surface responses at different Ag thickness.
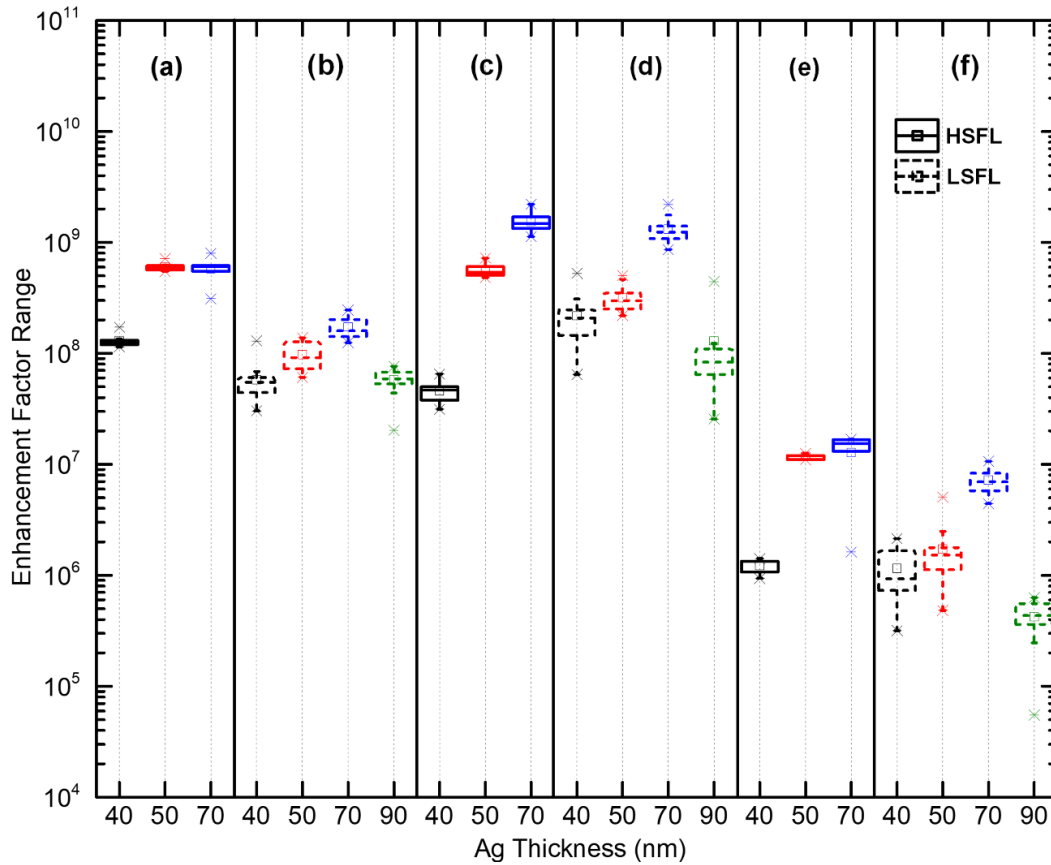
Figure 4.7 Box charts displaying enhancement factor results of both Si-HSFL and Si-LSFL substrates for varying Ag thickness at 532, 660 and 785 nm Raman excitation wavelengths.

4.5   Intensity Range & Enhancement Factor Results of Ti-LSFL Substrates

Different processing powers are tested to investigate structural change of Ti-LSFL structures. SEM images of these substrates reveal that increasing power results increase in irregularities of Ti-LSFL structures. Related SERS intensity ranges in Figure 4.8 shows that increased irregularity of Ti-LSFL results higher signal amplification and larger signal variance. Nathan's SERS uncertainty principle in *Chapter 1* is confirmed by these results. Periodicities of nanoripples are enlarged for higher processing power even if there is no drastical increase since the irradiation

wavelength remains same for the Ti-LSFL formation. Widened periodicities are the reason for decreasing SERS signal amplification. However higher and randomly distributed discontinuities are observed for high power Ti-LSFL structures which is responsible for larger SERS amplification compared to homogeneous Ti-LSFL structures fabricated at low processing power. Similar to Si-LSFL intensity ranges, highest ranges are observed at 660 nm excitation wavelength while lowest intensity ranges for 785 nm excitation wavelength.
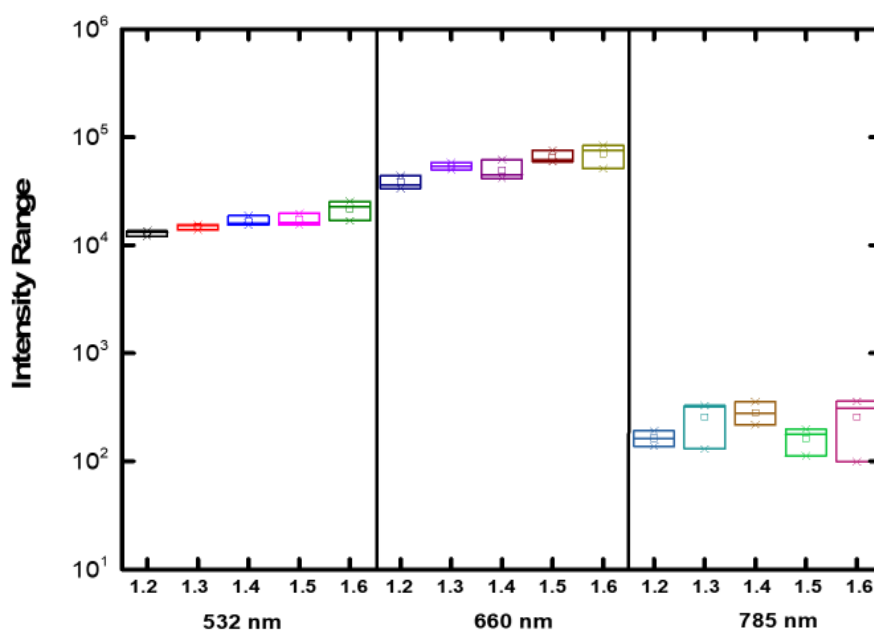
Figure 4.8 Box charts displaying the statistics of SERS measurements for 532,660 and 785 nm Raman excitation wavelength for the peak 1372 cm^{-1} of 10^{-5} M CV on 30 nm Ag coating; *Ti-LSFL with different processing powers at 8m/s; 1.2 W; 1.3 W; 1.4 W; 1.5 W; 1.6 W.*
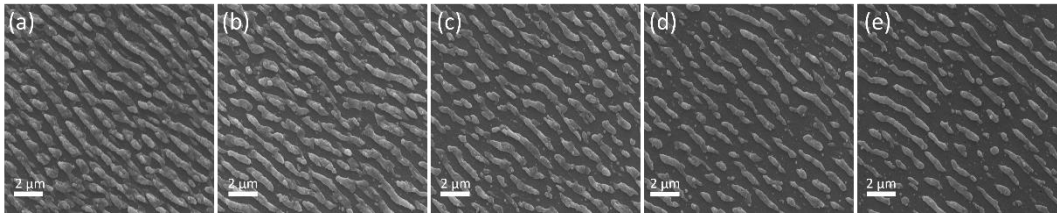
Figure 4.9 SEM images of Ti-LSFL obtained by different processing powers (a) 1.2 W, (b) 1.3W, (c) 1.4 W, (d) 1.5 W, (e) 1.6 W, hatch distance 4 μm, processing speed 8 m/s.

Box charts displaying SERS intensity range of 30 nm Ag coated Ti-LSFL structures obtained with different processing speeds are demonstrated in Figure 4.10 for three Raman excitation wavelengths. Maximum intensity range is observed at 660 nm Raman excitation wavelength.
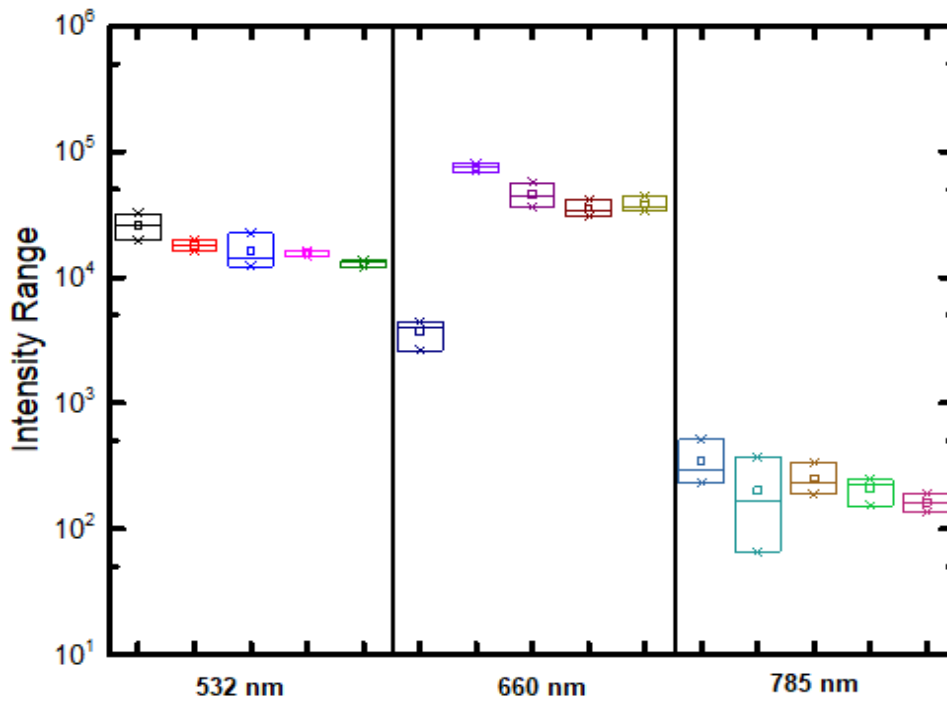
Figure 4.10 Box charts displaying the statistics of SERS measurements for 532,660 and 785 nm Raman excitation wavelength for the peak 1372 cm^{-1} of 10^{-5} M CV on 30 nm Ag coating; *Ti-LSFL with different processing speeds at 1.2 W; 4 m/s, 5 m/s; 6 m/s; 7 m/s; 8 m/s.*

4.6 Limit of Detection Values of SERS Substrates

As we discussed before, SERS is a powerful analytical technique that allows discrimination between presence or absence of analyte for extremely low concentrations. To determine detection sensitivity of the generated SERS substrates, CV concentration dependence of the SERS signal between 10^{-5}-10^{-11} M on 50 nm Ag coated Si-HSFL and 70 nm Ag coated Si-LSFL substrates are investigated at 532 and 660 nm Raman excitation wavelengths (Figure 4.11) and (Figure 4.12).
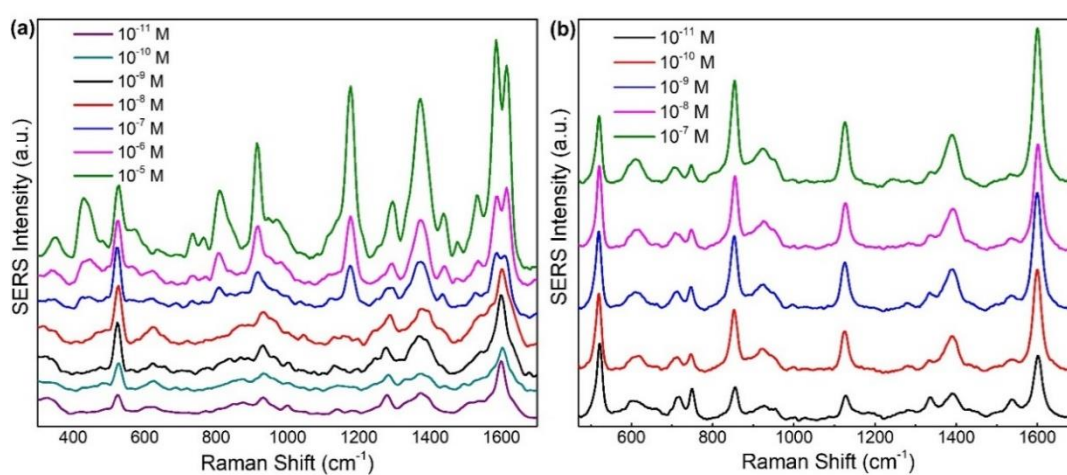
Figure 4.11 CV concentration dependence of SERS signal for 50 nm Ag coated Si-HSFL structures at Raman excitation (a) 532 nm, (b) 660 nm.
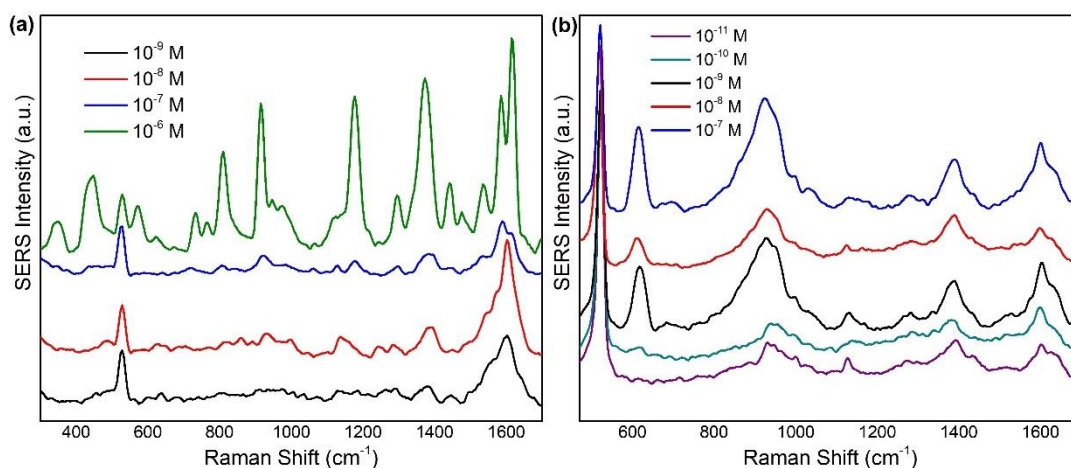
Figure 4.12 CV concentration dependence of SERS signal for 70 nm Ag coated Si-LSFL structures at Raman excitation (a) 532 nm, (b) 660 nm.

During low CV concentration measurements performed at 532 nm for 50 nm Ag coated Si-HSFL, most prominent and characteristic four peaks of CV are identified and assigned as follows: ring skeletal vibrations (940 cm^{-1}), ring C-C stretching (1295 cm^{-1}), N-phenyl stretching (1374 cm^{-1}), C-C stretching (1615 cm^{-1}). Identification of additional characteristic peaks is observed for 10^{-11} M CV at 660 nm excitation. This observation is consistent with higher enhancement factor value presented at 660 nm relative to 532 nm Raman excitation for Si-HSFL and Si-LSFL structures. All CV peaks with their related band assignments are listed in Table 4.2 [91,92]. CV modes appear at low CV concentration on SERS substrates at 532 nm Raman excitation is written in italic.

Table 4.2 Set of CV peaks with their related band assignments.

Band assignments	CV peaks (cm^{-1})
C^+-phenyl bending	348
Out of plane ring C-C bending	434
Ring skeletal vibration of radical orientation	528
Out of plane C-H bending	732, 760
Out of plane ring C-H bending	815
Ring skeletal vibrations	*940*
C-C stretching	1586, *1615*
Plane ring C-H bending	1177
N-phenyl stretching	*1374*
Ring C-C stretching	1295, 1535
Ring C-C stretching ring deformation	1446

By calculating integrated SERS intensity results for the CV peak located at 1374 cm^{-1} for the varying CV concentrations, LoD lines and LoD values of the SERS substrates are given in Figure 4.13 and Table 4.3, respectively. The N- phenyl stretching peak is detected down to 10^{-11} M with a good signal to noise ratio.
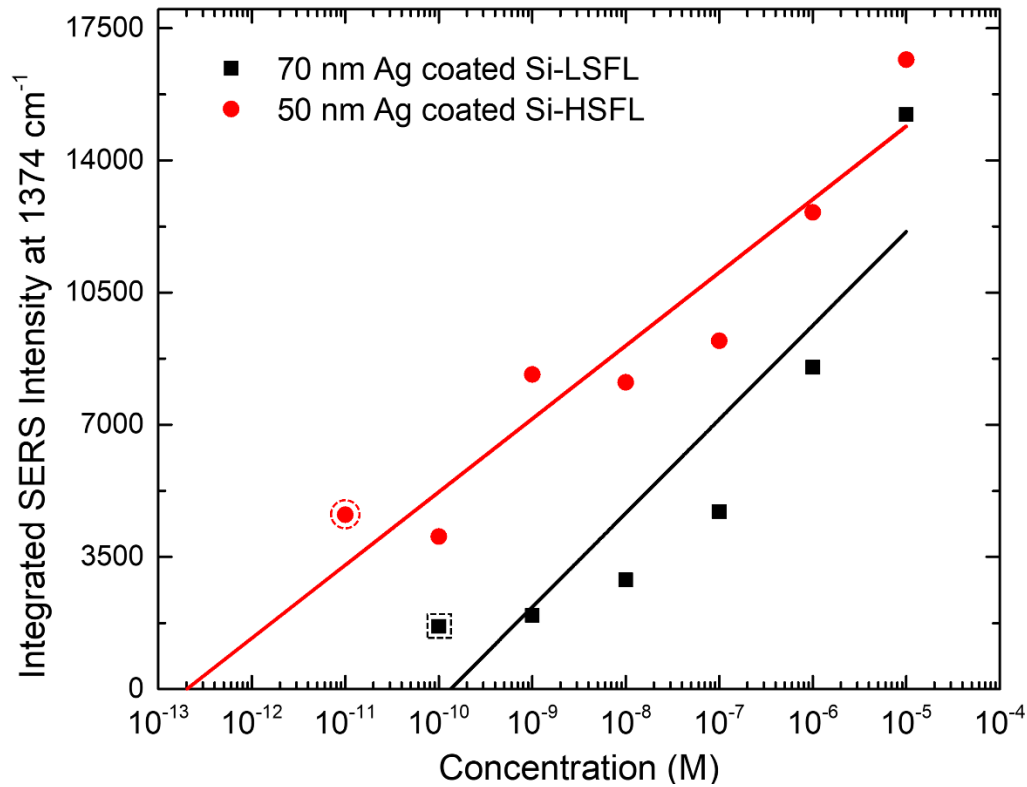
Figure 4.13 Limit of Detection lines of the SERS Substrates.

Table 4.3 Limit of Detection Values of SERS Substrates

Raman excitation	*532 nm*	*660 nm*
Si-HSFL	10^{-11}	10^{-11}
Si-LSFL	10^{-10}	10^{-11}

4.7   Reflection Measurements of Si-LSFL and Si-HSFL Substrates

The reflection spectra for the Si-LSFL and Si-HSFL structures are shown in Figure 4.14 and Figure 4.15 respectively. The coupling of the photon to the SPPs and scattered photon in all directions contributes the observed reflection spectra. By

considering increased optical path and light trapping effect presented by both types of LIPSS structures, one may expect to observe decreased reflectance of textured Si substrate, but a differing Ag deposition increases it again. Increasing Ag thickness leads to planarized nanoripples and reflectance increases proportionally with increasing Ag thickness. Ag coated LIPSS samples exhibit decreased reflectance in the visible wavelength range with respect to flat Ag spectra. This case may guide towards additional SPP coupling loss.
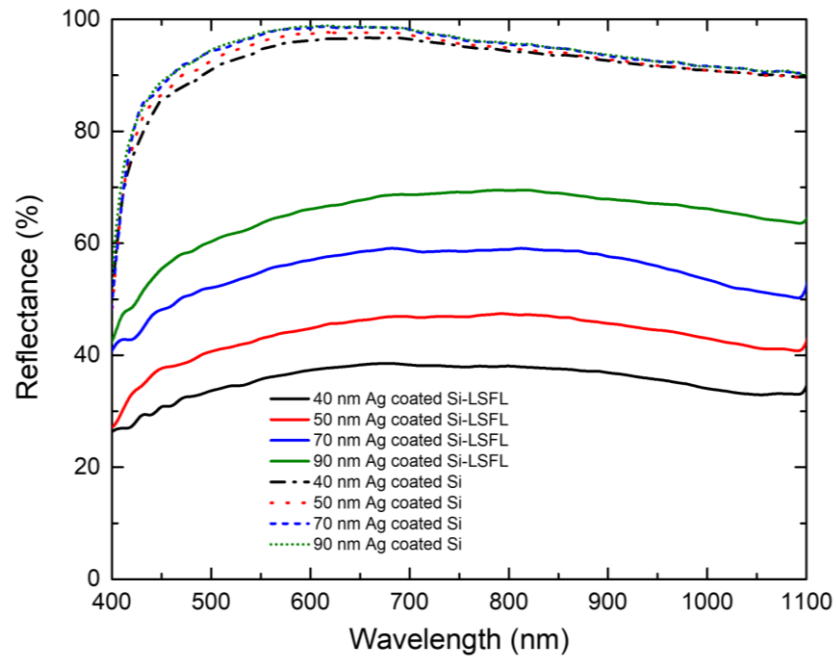
Figure 4.14 Reflectance measurements with varying Ag thickness of the Si-LSFL structures (dashed spectra are obtained from varying Ag thickness on flat Si wafer for comparison).
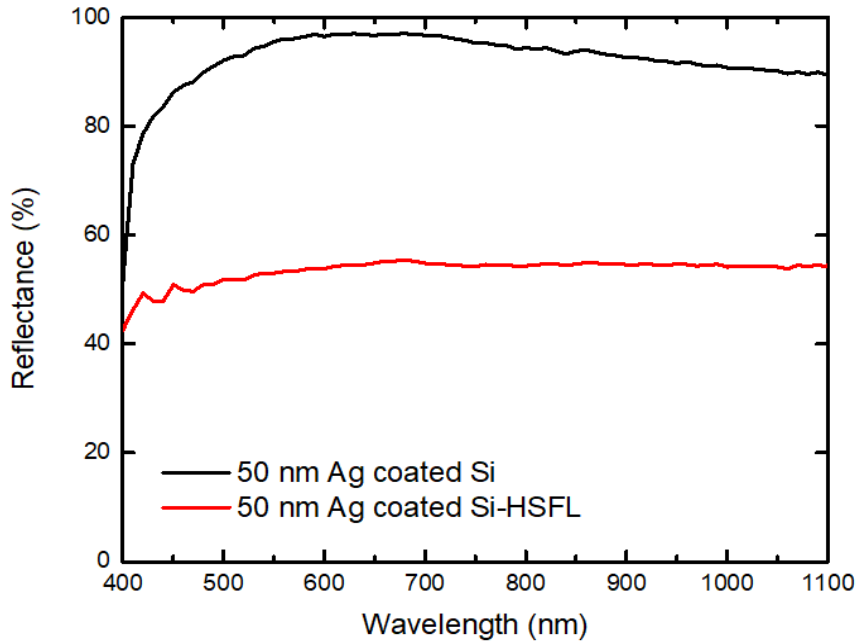
Figure 4.15 Reflectance measurement of 50 nm Ag coated Si-HSFL structure (in red) and 50 nm Ag coated flat Si wafer (in black).

Introduction of the surface gratings and surface roughness are most employed strategies among alternative methods of SPPs excitation. Excitations of SPPs can be also performed by fibre tip coupling, point defect scattering and electronic stimulation [93]. Kretschmann configuration reports penetration depth in the noble materials between 10-15 nm for the 500-700 nm wavelength range [94]. Presented configuration in our study does not restrict the coupling of light to surface plasmons for some specific angles or frequencies, but covers the nanoroughness of the periodic patterns. Absorption and penetration depth increase with increasing nanoroughness [95]. Furthermore, Raman measurements are perfomed by 100Z/0.90 NA objective in conjunction with multimode laser delivery fiber. Depths of focus in several tens of micrometers order ($r_z \cong 30$ μm) with 17 μm spot size. Therefore, crystalline Si phonon bands can be observed in spectra. Hence, we can see the crystalline Si phonon bands in the spectra. On the other side, Ag coated flat surfaces has reflectance higher than 90% across 400-700 nm wavelength range where it can be considered opaque at the Raman excitations wavelengths. In Figure 4.16, Raman

spectra of Ag coated Si wafer at 532 nm Raman excitation wavelength are demonstrated and Si phonon band at 521 cm^{-1} is absent.
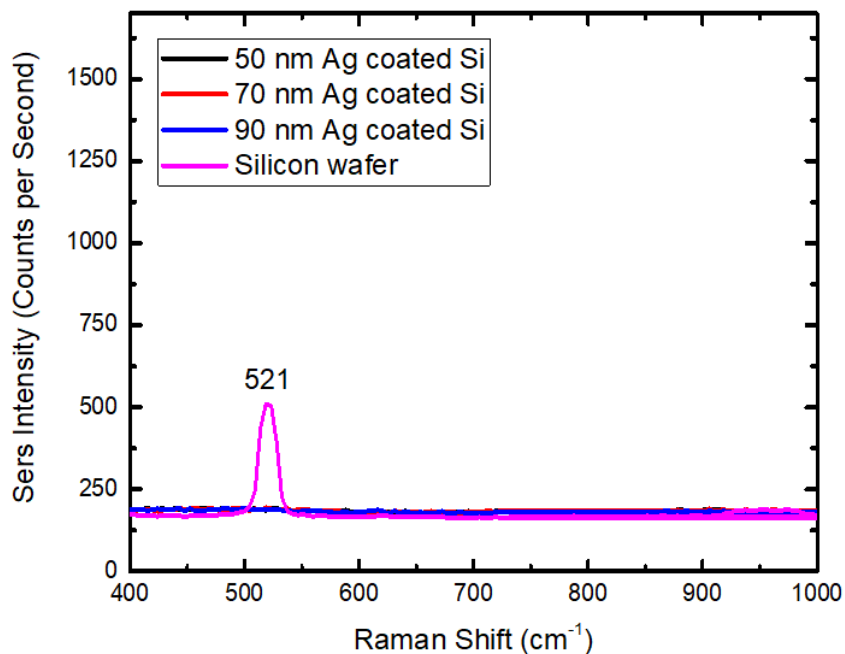
Figure 4.16 Raman spectra of 50 nm, 70 nm and 90 nm Ag coated Si wafer excited at 532 nm.

4.8 Raman Mapping Results

To test the uniformity of the SERS signal for 50 nm Ag deposited, 10^{-5} M CV coated Si-HSFL and 70 nm Ag deposited, 10^{-5} M CV coated Si-LSFL structures micro-Raman measurements and related Raman mapping analysis are performed for three Raman excitation wavelengths 532, 633 and 785 nm over a 2.40 x 10^{-4} mm^2 area. The normalized SERS signal variation of N-phenyl stretching band 1374 cm^{-1} of CV molecule is particularly selected for all analysis to avoid fitting errors by dominant existence of the peak which is observed for even at low concentration of CV. The area under the dominant peak of the CV molecule I_{SERS} is calculated for each pixel.

Coordinate dependent signal variance calculated 24% for Si-LSFL and 27% for the Si-HSFL (Figure 4.17) at 532 nm Raman excitation. 10^{-5} M CV spin-coated and Ag thickness optimized SERS substrates are used. Signal variance obtained only for the 290 nm HSFL periodicities by eliminating hatch distance periodicities, variance is calculated as 15% (Figure 4.18). 5 µm hatch distance of the Si-HSFL structure is distinguishable in Figure 4.17a.
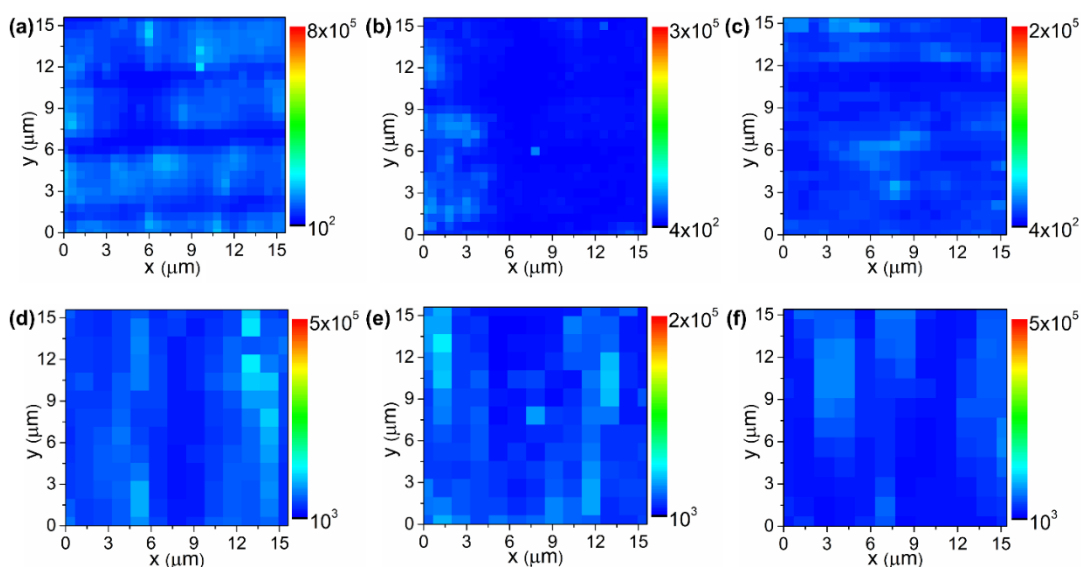
Figure 4.17 Normalized SERS signal variation of N-phenyl stretching band of CV for 70 nm Ag, 10^{-5} M CV Si-HSFL structures at Raman excitation a) 532 nm, b) 633 nm, c) 785 nm. Normalized SERS signal variation of 70 nm Ag, 10^{-5} M CV coated Si-LSFL structures at Raman excitation wavelength.
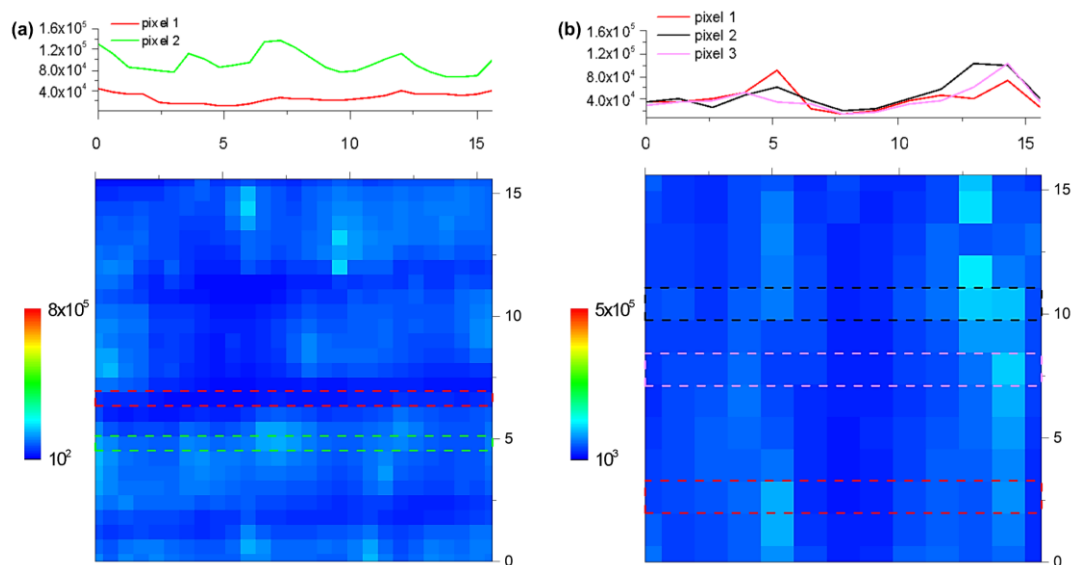
Figure 4.18 SERS signal variation on different locations of the 50 nm Ag deposited Si-HSFL structure 10^{-5} M CV (a), 70 nm Ag deposited Si-LSFL structure 10^{-5} M CV (b). Raman excitation wavelength is 532 nm for both substrates.

4.9 Raman Enhancement Factor Simulations

We previously mentioned that both incoming and outgoing field are amplified and an approximation $|E(\lambda_{excitation})|^4$ related with Raman Field Enhancement in Equation 1.26 is used. This approximation is used in Raman enhancement factor simulations and only covers the field enhancement mechanisms of the SERS. Therefore, contribution of charge transfer between CV analyte and Ag coated surface and polarizability change of the CV molecule are excluded. Enhancement factor for 50 nm Ag coated Si-HSFL structures and 70 nm Ag coated Si-LSFL structures are given in Table 4.4. As we can expect with the lightning rod effect aforementioned in *Chapter 1*, highly localized field enhancements are observed at sharp tips and corners of the SERS substrates (Figure 4.19).

Table 4.4 Enhancement factor for Si-HSFL structures and Si-LSFL SERS substrates.

Wavelength (nm)	532	660	785
Si-HSFL	5.3×10^{13}	3.0×10^{13}	3.5×10^{13}
Si-LSFL	1.6×10^{11}	1.8×10^{12}	5.4×10^{9}
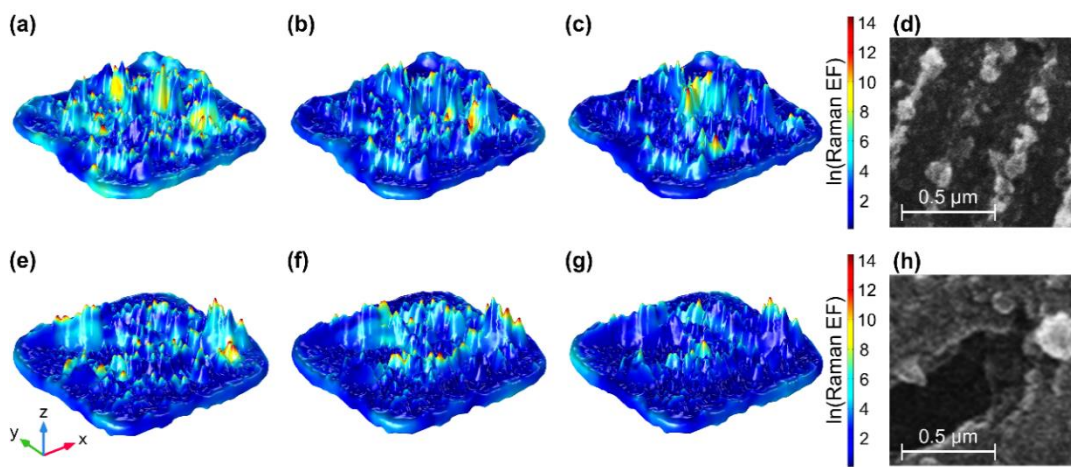
Figure 4.19 Field enhancement results of 50 nm Ag coated Si-HSFL structures illuminated at 532, 660 and 785 nm wavelengths respectively (a-c). Imported SEM image of bare Si-HSFL structure (d). Field enhancement results of 70 nm Ag coated Si-LSFL structures illuminated at 532, 660 and 785 nm wavelengths respectively (e-g). Imported SEM image of the bare Si-LSFL structure (h). Scale is chosen as logarithmic to emphasize hot spots arising from lightning rod effect.

Mesh models are given in Figure 4.20 for the nanoripples. The resolution of the SEM images is slightly larger than 5 nm (each pixel spans an area of 5.81 nm x 5.81 nm). After the SEM images are imported, a linear interpolation is automatically performed so that the mesh is fine enough to capture the details of the structures. The height information is obtained by scaling the contrast of the SEM image according to AFM height measurements.
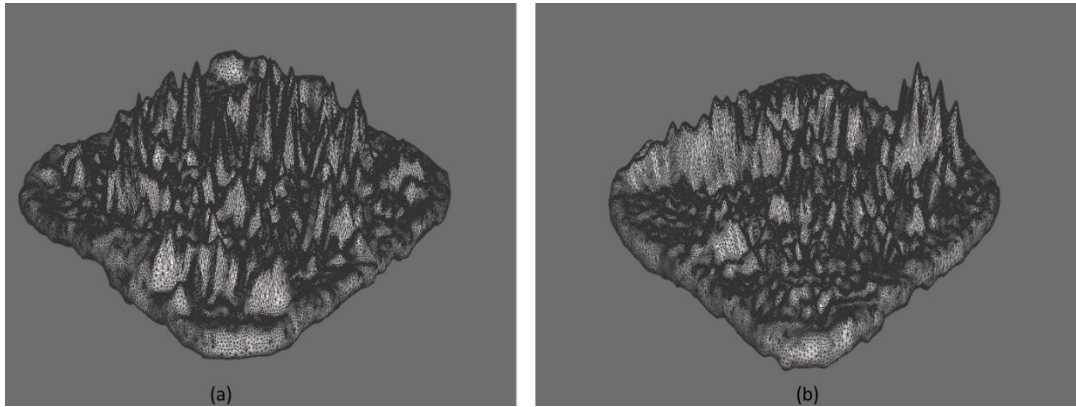
Figure 4.20 a) HSFL structure 3D view, generated using Meshmixer b) LSFL structure 3D view.

Polarization angle dependence of the calculated enhancement factor results are investigated for both 50 nm Ag deposited Si-HSFL and 70 nm Ag deposited Si-LSFL (Figure 4.21). Order difference observed for Si-LSFL structures between three excitation wavelengths is consistent with experimentally reported enhancement factors. Polarization dependence of the Si-LSFL structures is lower and wavelength dependence is higher than Si-HSFL structures.
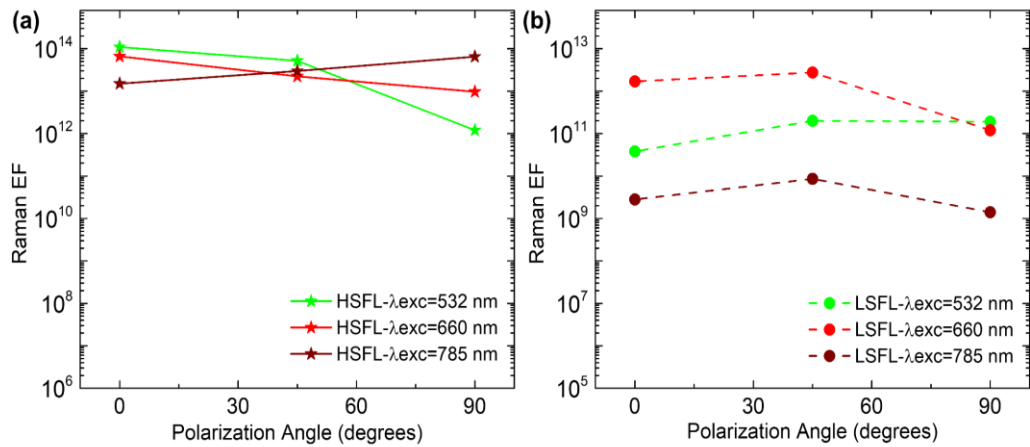
Figure 4.21 Raman enhancement factor results for different polarization angles for HSFL structures (a), LSFL structures (b).

4.10 Dark Field Scattering Spectra of Si-LSFL and Si-LSFL Substrates

Even if we present analytical tool to observe near field contributions by SERS, we previously mentioned in *Chapter 1* that LSPs coupled at a far field can profoundly increase the quality factor of a resonance. This case requires proper determination of periodic array, size and morphology of the metallic nanoparticles. To estimate the total contribution of far field couplings and to test their consistency with overall field enhancements obtained by SERS measurements and calculated field enhancements by COMSOL, we present dark field scattering spectra of both Si-HSFL and Si-LSFL structures. Although Abbe's diffraction limit prohibits the observation of the near field by far field dedicated instrument, when plasmon resonances including dipole modes predominantly contribute the far field can represent the near field. Nevertheless, this is not applicable for the higher order modes and correlation between them is lost. Dark field scattering plots provided in Figure 4.22 at Raman excitation and Raman scattering wavelength allow comparison of Raman EF improvement of each substrate relative to the Raman excitation wavelengths of 532, 660 and 785 nm (Table 4.5).
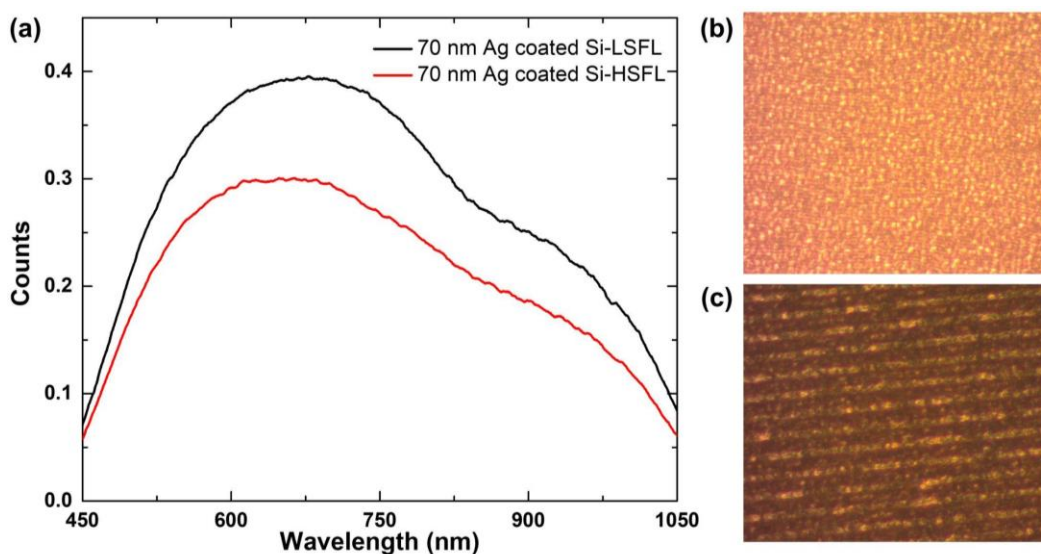
Figure 4.22 Dark field scattering spectra of 70 nm Ag coated Si-HSFL and Si-LSFL structures (a), dark field image of 70 nm Ag coated Si-LSFL (b), 70 nm Ag coated Si-HSFL.

N-phenyl stretching Raman band at 1375 cm^{-1} of the CV was used in calculations. Total intensities for each excitation wavelength were obtained by product of intensities related with Raman excitation and Raman scattering wavelength. Wavelength dependence of total intensities obtained at the field enhancement table has correlation between wavelength dependence of SERS enhancement factor ranges obtained in Figure 4.7 for 70 nm Ag coated Si-HSFL and Si-LSFL structures. Highest field enhancement of both types of structures were observed at 70 nm Ag thickness and 660 nm Raman excitation wavelength, which also correlates well with SERS results. Dark field scattering intensities correspond only to far-field components of the actual fields and do not correspond (and are not expected to) to the near field intensities where coupling of high order resonances to far field is hampered and dipole like ones are not.

Table 4.5 Dark field scattering intensities related with Raman excitation and Raman scattering wavelength.

	Excitation			Raman Scattering			Total		
Intensity$^)$	I_{E1}	I_{E2}	I_{E3}	I_{R1}	I_{R2}	I_{R3}	I_{T1}	I_{T2}	I_{T3}
Wavelength [nm]	532	660	785	573	725	879	532	660	785
Si-LSFL	0.72	0.98	0.85	0.87	0.97	0.72	0.62	0.95	0.61
Si-HSFL	0.74	0.98	0.91	0.90	0.92	0.63	0.66	0.90	0.51

4.11 Varying Laser Processing Parameters for Si-LSFL Substrates

Laser processing speed dependent SERS intensity ranges for the Si are not covered in this thesis. However, we included collective contribution of four different processing speeds used during Si nanostructuring. 5 different Raman spectrum is collected for each substrate obtained with 4 different processing speed 3 m/s, 5 m/s, 7 m/s and 10 m/s. SEM images are given in Figure 4.23. 20 spectra for each LSFL structure are collected.
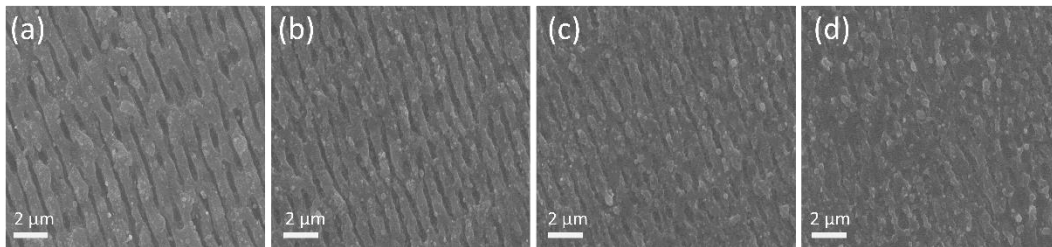
Figure 4.23 SEM images of Si-LSFL structures obtained with 3 m/s (a), 5 m/s (b), 7 m/s (c), 10 m/s (d), hatch distance is 4μm.

4.12   SERS Measurements of Brilliant Cresyl Blue (BCB) Molecule

SERS performance of another widely used Raman reporter, Brilliant Cresyl Blue (BCB) is investigated. SERS spectra of the 50 nm Ag coated, 10^{-5} M BCB spin-coated samples at 532 and 660 nm Raman excitation wavelengths are given in Figure 4.24.
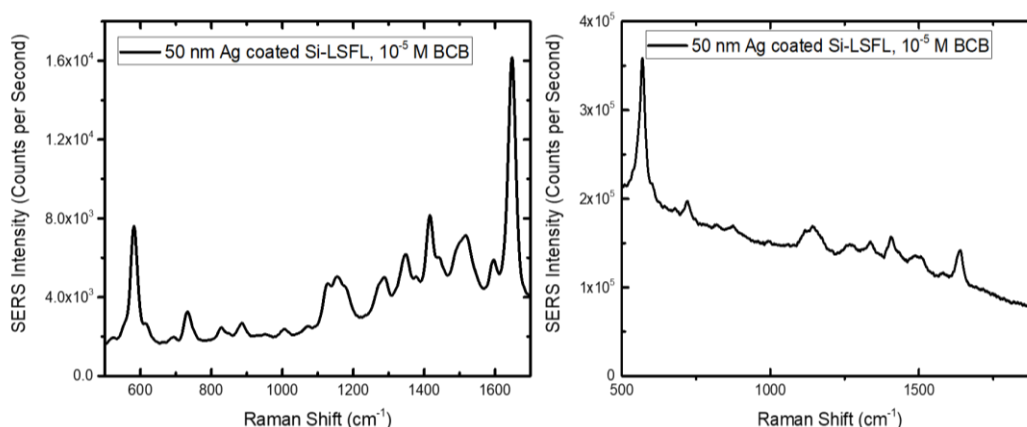
Figure 4.24 SERS spectra of 50 nm Ag coated and BCB spin coated Si-LSFL structures at Raman excitation (a) 532 nm, (b) 660 nm.

4.13   Future Studies for Comparison of Different Nano-Structuring Techniques

We consistently attempted to investigate femtosecond laser written SERS substrates and we presented state-of-art SERS performance results in this thesis. Moreover, recent studies focused on fs-laser nanostructuring based SERS substrates and direct laser writing also aim improved enhancement factors to achieve single molecule detection sensitivity [96-98]. Our attempt also motivates us to looking for alternative SERS generation techniques. Lastly, we would like to briefly mention formation of three-dimensional SERS substrates by metal assisted chemical etching (MACE). These experiments can provide competitive and promising method for SERS substrate generation. Also, they allow comparison of SERS substrates produced by

different nano structuring techniques. This comparison is beyond the scope of this thesis, but it may pave the way of our future studies about three-dimensional SERS substrate generation. Three-dimensional hot spot volume is introduced by nanowires and nano cones by MACE to achieve much more efficient use of Raman probe volume. Formation itself relies on Ag nanoparticle formation and oxidization of them. Metal salt $AgNO_3$ is used. Figure 4.25 and Figure 4.26 illustrate nanostructure formation by MACE with different oxidative agents and etching solutions. Two different oxidative agents are used HNO_3 or H_2O_2 during MACE process. Different oxidative agents, and ratio of reductive solution and oxidative solutions differs resulting shapes of the nanostructures. Lower etching ratio is obtained with HNO_3 compared to H_2O_2.
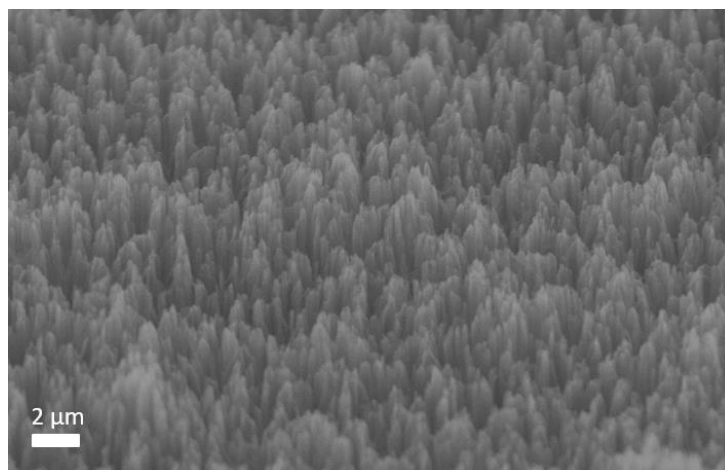
Figure 4.25 SEM images of nanostructures obtained by MACE using oxidative agent H_2O_2. Etching duration is 8 minutes.
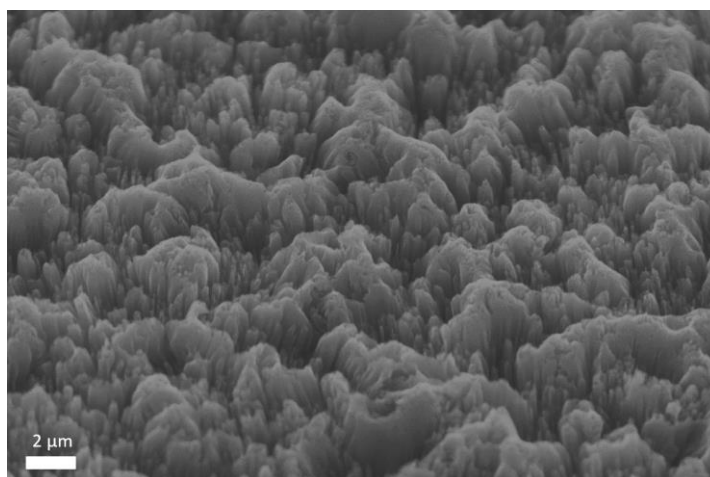
Figure 4.26 SEM images of nanostructures obtained by MACE using oxidative agent HNO$_3$. Etching duration is 60 minutes.

Even if MACE nanostructures obtained with oxidative agent H$_2$O$_2$ and metal salt AgNO$_3$ present larger uniformity than structures obtained with oxidative agent HNO$_3$, uniform nano structuring over large areas are very limited with MACE technique compared to femtosecond laser writing. Since wet chemical etching procedures are followed by MACE, freedom to process specific regions for nanostructuring is lost. However, it is important to note that MACE techniques intrinsically involve the use plasmonic materials. Typically, Ag and Au residues after the process are unwanted for the solar cell device applications and removed by HNO$_3$ but for the SERS applications their existence is crucial and allows us to obtain SERS substrates in one pot wet chemical process. SERS spectrum of 40 nm Ag coated MACE nanostructures obtained with different etching durations are demonstrated in Figure 4.27. Highest SERS signal amplification is observed for shortest etching duration and therefore for the nano structures with lowest aspect ratio.
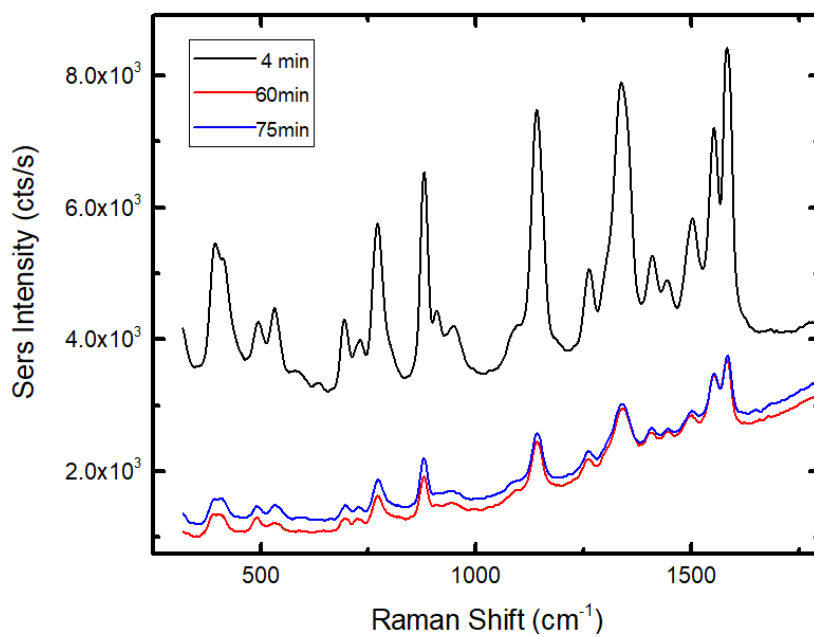
Figure 4.27 SERS spectrum of 40 nm Ag coated nanostructures formed by MACE, with an oxidative agent HNO_3.

CHAPTER 5

CONCLUSION

As a consequence of varying resonance conditions, highly localized electric field enhancements in the vicinity of the sharp ends, corners and reduced inter-particle spacings of the nanostructures are presented and they justify the strong morphology dependency of the SERS signal amplification. Amplified SERS signals are highly correlated with the capabilities of detecting analytes at low concentration or even single molecule detection. Femtosecond laser-based SERS substrates allow accurate and flexible control of processed regions without restricting processing over large areas. Time effective, versatile and substrate to substrate reproducible technique is presented without requiring multiple steps of nanofabrication. Laser assisted periodic nanopatterns with two different periodicity regimes are reported as a highly sensitive SERS substrate. One of the periodicities is correlated with laser irradiation wavelength, and the second one is correlated with the second harmonic of the laser irradiation wavelength. EF factor results with three different Raman excitation wavelengths (532, 660, 785 nm) and varying Ag thickness are considered. Optimized EF result is reported as 10^9 with the 10^{-11} LoD value for the CV molecule. Enhancement factor results obtained by measured SERS spectra and electric field enhancement simulations exhibit good agreement between them. As a speculative third approach to estimate field enhancement by presumption of predominant dipole mode contribution and neglected higher order mode contribution, dark field scattering spectra of the SERS substrates are analyzed. Overwiew and results of the three different approach to conlude SERS performance of the Si-HSFL and Si-LSFL structures is given in Figure 5.1.
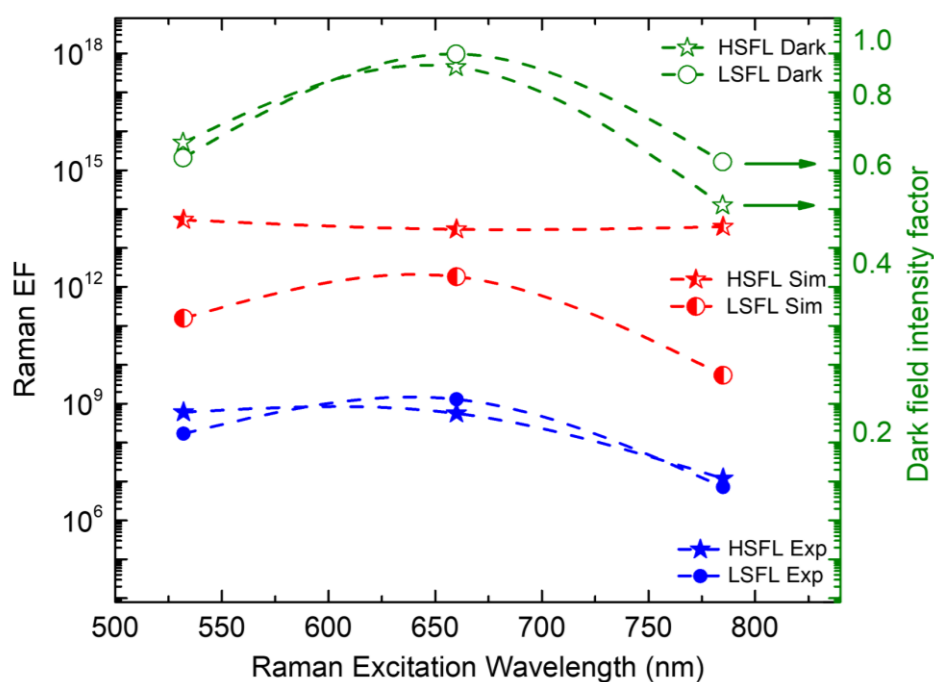
Figure 5.1 Experimental SERS EF results (blue), simulated field enhancement results (red), dark field scattering spectra for field enhancement estimation.

The SERS performance of the varying laser processing speeds and varying laser fluence values are investigated on the Si and Ti substrates. Due to intrinsic higher tendency of the SPP generation on Ti substrates, higher regularities observed for Ti substrates compared to Si-LSFL structures. SERS performance of Ti low spatial frequency structures are reported with lower EF values compared to Si structures. Uniformity of the amplified SERS signal for the dominant band of the CV molecule is investigated by Raman mapping analysis.

Nanoparticle and Quantum-dot decorated LIPSS-SERS sensors are ideal candidates for the future studies. Varying Ag/Au deposition angle on the nanoripples, generation of Ti-HSFL structures can be also analyzed. As a future study and different SERS substrate generation technique we shortly present MACE nanowires and nanocones for the effective use of Raman probe volume by creating three dimensional hotspot generation. Even if intrinsically used plasmonic materials used during the MACE process allow one pot SERS substrate generation technique,

uniformity and structuring over large areas is profoundly limited with respect to fs-based SERS substrates. On the contary of direct laser writing techniques, accuracy and flexibility to process some part of the device is completely lost since MACE is a wet chemical etching technique.

REFERENCES

[1] Ito, T., & Okazaki, S. (2000). Pushing the limits of lithography. *Nature*, *406*(6799), 1027–1031.

[2] Sreekanth, K. v, & Murukeshan, V. M. (2010). Effect of metals on UV-excited plasmonic lithography for sub-50 nm periodic feature fabrication. *Applied Physics A*, *101*(1), 117–120.

[3] Osipov, A. A., Iankevich, G. A., Speshilova, A. B., Osipov, A. A., Endiiarova, E. v, Berezenko, V. I., Tyurikova, I. A., Tyurikov, K. S., & Alexandrov, S. E. (2020). High-temperature etching of SiC in SF6/O2 inductively coupled plasma. *Scientific Reports*, *10*(1), 19977.

[4] Saviñon-Flores, F., Méndez, E., López-Castaños, M., Carabarin-Lima, A., López-Castaños, K. A., González-Fuentes, M. A., & Méndez-Albores, A. (2021). A Review on SERS-Based Detection of Human Virus Infections: Influenza and Coronavirus. *Biosensors*, *11*(3), 66.

[5] Lee, W., Kang, B.-H., Yang, H., Park, M., Kwak, J. H., Chung, T., Jeong, Y., Kim, B. K., & Jeong, K.-H. (2021). Spread spectrum SERS allows label-free detection of attomolar neurotransmitters. *Nature Communications*, *12*(1), 159.

[6] Anker, J. N., Hall, W. P., Lyandres, O., Shah, N. C., Zhao, J., & Van Duyne, R. P. (2008). Biosensing with plasmonic nanosensors. *Nature materials*, *7*(6), 442–453.

[7] Pyrak, E., Krajczewski, J., Kowalik, A., Kudelski, A., & Jaworska, A. (2019). Surface Enhanced Raman Spectroscopy for DNA Biosensors-How Far Are We? *Molecules (Basel,Switzerland)*, *24*(24),4423.

[8] Xu, M. L., Gao, Y., Han, X. X., & Zhao, B. (2022). Innovative Application of SERS in Food Quality and Safety: A Brief Review of Recent Trends. *Foods (Basel, Switzerland)*, *11*(14), 2097.

[9] Cheng, J., Zhang, S., Wang, S., Wang, P., Su, X.-O., & Xie, J. (2019). Rapid and sensitive detection of acrylamide in fried food using dispersive solid-phase extraction combined with surface-enhanced Raman spectroscopy. *Food Chemistry*, *276*, 157–163.

[10] Wei, H., Hossein Abtahi, S. M., & Vikesland, P. J. (2015). Plasmonic colorimetric and SERS sensors for environmental analysis. In *Environmental Science: Nano* (Vol. 2, Issue 2, pp. 120–135). Royal Society of Chemistry.

[11] Yu, B., Ge, M., Li, P., Xie, Q., & Yang, L. (2019). Development of surface-enhanced Raman spectroscopy application for determination of illicit drugs: Towards a practical sensor. *Talanta*, *191*, 1–10.

[12] Raman, C. V. (1998). A new radiation [Reproduced from Indian J. Phys., 1928, 2, 387–398]. *Current Science*, *74*(4), 382–386

[13] Fleischmann, M., Hendra, P. J., & McQuillan, A. J. (1974). Raman spectra of pyridine adsorbed at a silver electrode. *Chemical Physics Letters*, *26*(2), 163–166.

[14] Jeanmaire, D. L., & Van Duyne, R. P. (1977). Surface Raman Spectroelectrochemistry. Part I. Heterocyclic, aromatic, and aliphatic amines adsorbed on the anodized silver electrode. *Journal of Electroanalytical Chemistry*, *84*(1), 1-20.

[15] *S. I. Maslovski, C. R. Simovski, "Purcell factor and local intensity enhancement in surface-enhanced Raman scattering," Nanophotonics, vol. 8, pp. 429-434, 2019.*

[16] Bai, S., Serien, D., Ma, Y., Obata, K., & Sugioka, K. (2020). Attomolar Sensing Based on Liquid Interface-Assisted Surface-Enhanced Raman Scattering in Microfluidic Chip by Femtosecond Laser Processing. *ACS Applied Materials & Interfaces*, *12*(37), 42328–42338.

[17] Nie, S., & Emory, S. R. (1997). Probing Single Molecules and Single Nanoparticles by Surface-Enhanced Raman Scattering. *Science (New York, N.Y.)*, *275*(5303), 1102–1106.

[18] Xu, K., Zhou, R., Takei, K., & Hong, M. (2019). Toward Flexible Surface-Enhanced Raman Scattering (SERS) Sensors for Point-of-Care Diagnostics. *Advanced Science*, *6*(16).

[19] Kneipp K, Wang Y, Kneipp H, Perelman L, Itzkan I, Dasari R and Feld M (1997) Single molecule detection using surface-enhanced Raman scattering (SERS) *Phys. Rev. Lett*. 78 1667–70.

[20] Fano, U. (1961). Effects of Configuration Interaction on Intensities and Phase Shifts. *Physical Review*, *124*(6), 1866–1878.

[21] E. Kretschmann. (1971) Die Bestimmung optischer Konstanten von Metallen durch Anregung von Oberflächenplasmaschwingungen," *Zeitschrift für Physik A Hadrons and Nuclei*, 241, 313-324.

[22] Raether, H. (1988) Surface Plasmons on Smooth and Rough Surfaces and on Gratings. *Springer*, Heidelberg.

[23] Kocabas, A., Dåna, A., & Aydinli, A. (2006). Excitation of a surface plasmon with an elastomeric grating. *Applied Physics Letters*, *89*(4).

[24] *Hot spots*. SERS Substrates - Gold and silver for molecular detection. (n.d.). Retrieved November 9, 2022, from https://www.silmeco.com/knowledge-base/hot-spots/

[25] Wang, L. (n.d) Excitation of surface plasmon polaritions at the silver-air interface in Kretschmann-Raether configuration - Tutorial model for COMSOL/LFW webinar "Modeling Optoelectronic Devices and Plasmon Effects".

[26] Lilley, G., Messner, M., & Unterrainer, K. (2015). Improving the quality factor of the localized surface plasmon resonance. *Optical Materials Express*, *5*(10), 2112–2120.

[27] Han, H., Fang, Y., Li, Z., & Xu, H. (2008). Tunable Surface Plasma Resonance Frequency in Ag core/Au shell nanoparticles system prepared by laser ablation. *Applied Physics Letters*, *92*(2).

[28] Starowicz, Z., Wojnarowska-Nowak, R., Ozga, P., & Sheregii, E. M. (2018). The tuning of the plasmon resonance of the metal nanoparticles in terms of the SERS effect. *Colloid and Polymer Science*, *296*(6), 1029–1037.

[29] Liao, P. F., & Wokaun, A. (1982). Lightning rod effect in surface enhanced Raman scattering. In *The Journal of Chemical Physics* (Vol. 76, Issue 1, pp. 751–752).

[30] Wang, R., Ma, J., Dai, X., Gao, Y., Gu, C., & Jiang, T. (2023). Highly active SERS chip with both structure-ameliorated chemical enhancement and nanocavity-mediated electromagnetic enhancement. *Sensors and Actuators B: Chemical*, *374*, 132782.

[31] Christesen, S. D. (1988). Raman Cross Sections of Chemical Agents and Simulants. *Applied Spectroscopy*, *42*(2), 318–321.

[32] Zhang, M., Sun, H., Chen, X., Yang, J., Shi, L., Chen, T., Bao, Z., Liu, J., & Wu, Y. (2019). Highly Efficient Photoinduced Enhanced Raman Spectroscopy (PIERS) from Plasmonic Nanoparticles Decorated 3D Semiconductor Arrays for Ultrasensitive, Portable, and Recyclable Detection of Organic Pollutants. *ACS Sensors*, *4*(6), 1670–1681.

[33] Glass, D., Cortés, E., Ben-Jaber, S., Brick, T., Peveler, W. J., Blackman, C. S., Howle, C. R., Quesada-Cabrera, R., Parkin, I. P., & Maier, S. A. (2019). Dynamics of Photo-Induced Surface Oxygen Vacancies in Metal-Oxide Semiconductors Studied Under Ambient Conditions. *Advanced Science*, *6*(22), 1901841.

[34] Fang, Y., Seong, N. H., & Dlott, D. D. (2008). Measurement of the distribution of site enhancements in surface-enhanced Raman scattering. *Science (New York, N.Y.)*, *321*(5887), 388–392.

[35] Natan M. J. (2006). Surface enhanced Raman scattering. *Faraday discussions*, *132*, 321–328.

[36] Chan, T.-Y., Liu, T.-Y., Wang, K.-S., Tsai, K.-T., Chen, Z.-X., Chang, Y.-C., Tseng, Y.-Q., Wang, C.-H., Wang, J.-K., & Wang, Y.-L. (2017). SERS Detection of Biomolecules by Highly Sensitive and Reproducible Raman-Enhancing Nanoparticle Array. *Nanoscale Research Letters*, *12*(1), 344.

[37] Majumdar, D., Jana, S., & Kumar Ray, S. (2022). Gold nanoparticles decorated 2D-WSe$_2$ as a SERS substrate. *Spectrochimica acta. Part A, Molecular and biomolecular spectroscopy*, *278*, 121349.

[38] Sha, P., Su, Q., Dong, P., Wang, T., Zhu, C., Gao, W., & Wu, X. (2021). Fabrication of Ag@Au (core@shell) nanorods as a SERS substrate by the oblique angle deposition process and sputtering technology. *RSC advances*, *11*(44), 27107–27114.

[39] Sheng, W., Li, W., Tan, D., Zhang, P., Zhang, E., Sheremet, E., Schmidt, B. V. K. J., Feng, X., Rodriguez, R. D., Jordan, R., & Amin, I. (2020). Polymer Brushes on Graphitic Carbon Nitride for Patterning and as a SERS Active Sensing Layer via Incorporated Nanoparticles. *ACS applied materials & interfaces*, *12*(8), 9797–9805.

[40] Francis, M. K., Sahu, B. K., Bhargav, P. B., C, B., Ahmed, N., Das, A., & Dhara, S. (2022). Ag nanowires-based SERS substrates with very high enhancement factor. *Physica E: Low-Dimensional Systems and Nanostructures*, *137*, 115080.

[41] Liu, Y., Wu, S.-H., Du, X.-Y., & Sun, J.-J. (2021). Plasmonic Ag nanocube enhanced SERS biosensor for sensitive detection of oral cancer DNA based on nicking endonuclease signal amplification and heated electrode. *Sensors and Actuators B: Chemical*, *338*, 129854.

[42] Kim, S., Kim, T. G., Lee, S. H., Kim, W., Bang, A., Moon, S. W., Song, J., Shin, J. H., Yu, J. S., & Choi, S. (2020). Label-Free Surface-Enhanced Raman Spectroscopy Biosensor for On-Site Breast Cancer Detection Using Human Tears. *ACS applied materials & interfaces*, *12*(7), 7897–7904.

[43] Yuan, K., Zheng, J., Yang, D., Jurado Sánchez, B., Liu, X., Guo, X., Liu, C., Dina, N. E., Jian, J., Bao, Z., Hu, Z., Liang, Z., Zhou, H., & Jiang, Z. (2018). Self-

Assembly of Au@Ag Nanoparticles on Mussel Shell To Form Large-Scale 3D Supercrystals as Natural SERS Substrates for the Detection of Pathogenic Bacteria. *ACS Omega*, *3*(3), 2855–2864.

[44] Cinel, N. A., Cakmakyapan, S., Butun, S., Ertas, G., & Ozbay, E. (2015). E-Beam lithography designed substrates for surface enhanced Raman spectroscopy. *Photonics and Nanostructures - Fundamentals and Applications*, *15*, 109–115.

[45] Suresh, V., Ding, L., Chew, A. B., & Yap, F. L. (2018). Fabrication of Large-Area Flexible SERS Substrates by Nanoimprint Lithography. *ACS Applied Nano Materials*, *1*(2), 886–893.

[46] Wang, T.-J., Hsu, K.-C., Liu, Y.-C., Lai, C.-H., & Chiang, H. P. (2016). Nanostructured SERS substrates produced by nanosphere lithography and plastic deformation through direct peel-off on soft matter. *Journal of Optics*, *18*, 055006.

[47] Barcelo, S. J., Wu, W., Li, X., Li, Z., & Williams, R. S. (2015). Nanoimprint lithography of plasmonic platforms for SERS applications. *Applied Physics A*, *121*(2), 443–449.

[48] Sivashanmugan, K., Liao, J.-D., & Liu, B. H. (2015). Focused-ion-beam-fabricated homogeneous acute-angled Au nanorods for surface-enhanced Raman scattering. Applied Physics Express, 8(5), 052402.

[49] Zhang, C., Chen, S., Jiang, Z., Shi, Z., Wang, J., & Du, L. (2021). Highly Sensitive and Reproducible SERS Substrates Based on Ordered Micropyramid Array and Silver Nanoparticles. *ACS Applied Materials & Interfaces*, *13*(24), 29222–29229.

[50] Sun, X., Wang, N., & Li, H. (2013). Deep etched porous Si decorated with Au nanoparticles for surface-enhanced Raman spectroscopy (SERS). *Applied Surface Science*, *284*, 549–555.

[51] Waiwijit, U., Chananonnawathorn, C., Eimchai, P., Bora, T., Hornyak, L., & Nuntawong, N. (2020). Fabrication of Au-Ag nanorod SERS substrates by co-sputtering technique and dealloying with selective chemical etching. *Applied Surface Science*, *530*, 147171.

[52] Ming, T., Dietzek-Ivanšić, B., Lu, X., Zuo, X., & Sivakov, V. (2022). Silicon Nanowires Decorated with Silver Nanoparticles for Photoassisted Hydrogen Generation. *ACS Applied Energy Materials*, *5*(6), 7466–7472.

[53] Ouhibi, A., Saadaoui, M., Lorrain, N., Guendouz, M., Raouafi, N., & Moadhen, A. (2020). Application of Doehlert Matrix for an Optimized Preparation of a Surface-Enhanced Raman Spectroscopy (SERS) Substrate Based on Silicon Nanowires for Ultrasensitive Detection of Rhodamine 6G. *Applied spectroscopy*, *74*(2), 168–177.

[54] Bai, S., Serien, D., Hu, A., & Sugioka, K. (2018). 3D Microfluidic Surface-Enhanced Raman Spectroscopy (SERS) Chips Fabricated by All-Femtosecond-Laser-Processing for Real-Time Sensing of Toxic Substances. *Advanced Functional Materials*, *28*, 1706262.

[55] Bai, S., Du, Y., Wang, C., Wu, J., & Sugioka, K. (2019). Reusable Surface-Enhanced Raman Spectroscopy Substrates Made of Silicon Nanowire Array Coated with Silver Nanoparticles Fabricated by Metal-Assisted Chemical Etching and Photonic Reduction. *Nanomaterials*, *9*, 1531.

[56] Hilal, H., Zhao, Q., Kim, J., Lee, S., Haddadnezhad, M., Yoo, S., Lee, S., Park, W., Park, W., Lee, J., Lee, J. W., Jung, I., & Park, S. (2022). Three-dimensional nanoframes with dual rims as nanoprobes for biosensing. *Nature Communications*, *13*(1), 4813.

[57] Anisimov, S. I., Kapeliovich, B. L., Perel'man, T. L., & Landau, L. D. (1975). *Electron emission from metal surfaces exposed to ultrashort laser pulses*.

[58] Sundaram, S. K., & Mazur, E. (2002). Inducing and probing non-thermal transitions in semiconductors using femtosecond laser pulses. *Nature materials*, *1*(4), 217–224.

[59] Majumdar, P., & Xia, H. (2007). A Green's function model for the analysis of laser heating of materials. *Applied Mathematical Modelling*, *31*(6), 1186–1200.

[60] Nolte, S., Momma, C., Jacobs, H., Tünnermann, A., Chichkov, B. N., Wellegehausen, B., & Welling, H. (1997). Ablation of metals by ultrashort laser pulses. *Journal of the Optical Society of America B, 14(10), 2716.*

[61] Radovanović, M., & Madić, M. (2011). Experimental investigations of CO2 laser cut quality: A review. *Nonconventional Technologies Review*, *15*.

[62] Naresh, & Khatak, P. (2022). Laser cutting technique: A literature review. *MaterialsToday: Proceedings*,*56*,2484–2489.

[63] Cao, X., Jahazi, M., Immarigeon, J. P., & Wallace, W. (2006). A review of laser welding techniques for magnesium alloys. *Journal of Materials Processing Technology*, *171*(2), 188–204.

[64] Chrisey, D. B., Piqué, A., McGill, R. A., Horwitz, J. S., Ringeisen, B. R., Bubb, D. M., & Wu, P. K. (2003). Laser Deposition of Polymer and Biomaterial Films. *Chemical Reviews*, *103*(2), 553–576.

[65] Majumdar, J. D., Nath, A. K., & Manna, I. (2004). Studies on laser bending of stainless steel. *Materials Science and Engineering: A*, *385*(1), 113–122.

[66] Montross, C. S., Wei, T., Ye, L., Clark, G., & Mai, Y.-W. (2002). Laser shock processing and its effects on microstructure and properties of metal alloys: a review. *International Journal of Fatigue*, *24*(10), 1021–1036.

[67] Saeidi, K., Gao, X., Zhong, Y., & Shen, Z. J. (2015). Hardened austenite steel with columnar sub-grain structure formed by laser melting. *Materials Science and Engineering: A*, *625*, 221–229.

[68] You, P., Li, G., Tang, G., Cao, J., & Yan, F. (2020). Ultrafast laser-annealing of perovskite films for efficient perovskite solar cells. *Energy & Environmental Science*, *13*(4), 1187–1196.

[69] Neuenschwander, B., Jaeggi, B., Schmid, M., & Hennig, G. (2014). Surface Structuring with Ultra-short Laser Pulses: Basics, Limitations and Needs for High Throughput. *Physics Procedia*, *56*, 1047–1058

[70] Verburg, P.C., Smillie, L.A., Römer, G.R., Haberl, B., Bradby, J.E., Williams, J.S., & Huis in 't Veld, A.J. (2015). Crystal structure of laser-induced subsurface modifications in Si. *Applied Physics A, 120*, 683-691.

[71] Bonse, J., Höhm, S., Kirner, S. v, Rosenfeld, A., & Krüger, J. (2017). Laser-Induced Periodic Surface Structures— A Scientific Evergreen. *IEEE Journal of Selected Topics in Quantum Electronics*, *23*(3), 1.

[72] Emmony, D. C., Howson, R. P., & Willis, L. J. (n.d.). Laser mirror damage in germanium at 106 μm. *Applied Physics Letters*, *23*(11), 598–600.

[73] Young, J. F., Sipe, J. E., & van Driel, H. M. (1984). Laser-induced periodic surface structure. III. Fluence regimes, the role of feedback, and details of the induced topography in germanium. *Phys. Rev. B*, *30*(4), 2001–2015.

[73] Young, J. F., Sipe, J. E., & van Driel, H. M. (1984). Laser-induced periodic surface structure. III. Fluence regimes, the role of feedback, and details of the induced topography in germanium. *Phys. Rev. B*, *30*(4), 2001–2015

[74] Sipe, J. E., Young, J. F., Preston, J. S., & van Driel, H. M. (1983). Laser-induced periodic surface structure. I. Theory. *Phys. Rev. B*, *27*(2), 1141–1154.

[75] Reif, J., Varlamova, O., Varlamov, S., & Bestehorn, M. (2011). The role of asymmetric excitation in self-organized nanostructure formation upon femtosecond laser ablation. *Applied Physics A*, *104*(3), 969–973.

[76] Vladimir I Emel'yanov, E M Zemskov, & V N Seminogov. (1984). Theory of the formation of "normal" and "anomalous" gratings on the surfaces of absorbing condensed media exposed to laser radiation. *Soviet Journal of Quantum Electronics*, *14*(11), 1515.

[77] Sipe, J.E., Driel, H.M.V., Young, J.F. (1985). Surface electrodynamics: radiation fields, surface polaritons, and radiation remnants. Canadian Journal of Physics 63, 104–113

[78] Abere, M., Torralva, B., & Yalisove, S. (2016). Periodic surface structure bifurcation induced by ultrafast laser generated point defect diffusion in GaAs. *Applied Physics Letters*, *108*, 153110.

[79] Höhm, S., Rosenfeld, A., Krüger, J., & Bonse, J. (2012). Femtosecond laser-induced periodic surface structures on silica. *Journal of Applied Physics*, *112*(1), 14901.

[80] Fang, Z., Zhao, Y.A., Shao, J. (2016). Femtosecond laser-induced periodic surface structure on fused silica surface. Optik 127, 1171–1175.

[81] Bonse, J., Rosenfeld, A., & Krüger, J. (2009). On the role of surface plasmon polaritons in the formation of laser-induced periodic surface structures upon irradiation of silicon by femtosecond-laser pulses. *Journal of Applied Physics*, *106*(10).

[82] Colombier, J.-P., Garrelie, F., Brunet, P., Bruyère, A., Pigeon, ff, Stoian, R., & Parriaux, O. (2012). Plasmonic and Hydrodynamic Effects in Ultrafast Laser-Induced Periodic Surface Structures on Metals. *Journal of Laser Micro / Nanoengineering*, *7*, 362–368.

[83] Mustafa, H., Matthews, D. T. A., & Römer, G. R. B. E. (2019). Investigation of the ultrashort pulsed laser processing of zinc at 515 nm: Morphology, crystallography and ablation threshold. *Materials & Design*, *169*, 107675.

[84] Yang, J. J., Liu, W. W., & Zhu, X. N. (2007). A study of ultrafast electron diffusion kinetics in ultrashort-pulse laser ablation of metals. *Chinese Physics*, *16*(7), 2003–2010.

[85] Varlamova, O., & Reif, J. (2013). Evolution of Femtosecond Laser Induced Surface Structures at Low Number of Pulses near the Ablation Threshold. *Journal of Laser Micro/Nanoengineering*, *8*, 300–303.

[86] Pavlov I., Yavuz O., Makey G. , Toker O. , Ilday O. *Switching between normal and anomalous Laser Induced Periodic Surface Structures,* (2017). Retrieved March 17, 2020, from the arXiv database.

[87] Dostovalov, A. V., Korolkov, V. P., & Babin, S. A. (2015). Simultaneous formation of ablative and thermochemical laser-induced periodic surface structures on Ti film at femtosecond irradiation. *Laser Physics Letters*, *12*(3).

[88] Tokel, O., Turnalı, A., Makey, G., Elahi, P., Çolakoğlu, T., Ergeçen, E., Yavuz, Ö., Hübner, R., zolfaghari borra, M., Pavlov, I., Bek, A., Turan, R., Kesim, D., Tozburun, S., Ilday, S., & Ilday, F. (2017). In-chip microstructures and photonic devices fabricated by nonlinear laser lithography deep inside silicon. *Nature Photonics*, *11*.

[89] Li, Z., Wu, Q., Jiang, X., Zhou, X., Liu, Y., Hu, X., Zhang, J., Yao, J., & Xu, J. (2022). Formation mechanism of high spatial frequency laser-induced periodic surface structures and experimental support. *Applied Surface Science*, *580*, 152107.

[90] Le Ru, E. C., Blackie, E., Meyer, M., & Etchegoin, P. G. (2007). Surface Enhanced Raman Scattering Enhancement Factors: A Comprehensive Study. *The Journal of Physical Chemistry C*, *111*(37), 13794–13803.

[91] Meng, W., Hu, F., Zhang, L. Y., Jiang, X. H., Lu, L. D., & Wang, X. (2013). SERS and DFT study of crystal violet. *Journal of Molecular Structure*, *1035*, 326–331.

[92] Persaud, I., & Grossman, W. E. L. (1993). Surface-enhanced Raman scattering of triphenylmethane dyes on colloidal silver. *Journal of Raman Spectroscopy*, *24*(2), 107–112.

[93] Zhang, J., Zhang, L., & Xu, W. (2012). Surface plasmon polaritons: Physics and applications. *Journal of Physics D-Applied Physics - 45*.

[94] Ru, E.C., & Etchegoin, P.G. (2008). Principles of Surface-Enhanced Raman Spectroscopy: And Related Plasmonic Effects.

[95] H. E. Bennett and J. O. Porteus. (1961). Relation Between Surface Roughness and Specular Reflectance at Normal Incidence, *Journal of Optial Society of. America*. 51, 123-129

[96] Hamad, S., Bharati Moram, S. S., Yendeti, B., Podagatlapalli, G. K., Nageswara Rao, S. V. S., Pathak, A. P., ... & Soma, V. R. (2018). Femtosecond Laser-induced, Nanoparticle-Embedded Periodic Surface Structures on Crystalline Silicon for Reproducible and Multi-utility SERS Platforms. *Acs Omega*, *3*(12), 18420-18432.

[97] Moram, S. S. B., Shaik, A. K., Byram, C., Hamad, S., & Soma, V. R. (2020). Instantaneous Trace Detection of Nitro-explosives and Mixtures with Nanotextured Silicon Decorated with Ag–Au alloy Nanoparticles Using the SERS Technique. *Analytica Chimica Acta*, *1101*, 157-168.

[98] Li, J., Mu, Y., Liu, M., & Zhang, X. (2022). Direct Laser Writing of SERS Hollow Fibers. *Nanomaterials, 12*(16), 2843.